Investigating radiation and its distribution in W7X with EMC3/EIRENE

Bachelor thesis

Philip Geißler

Universität Greifswald, Institut für Physik
University of Greifswald, Institute of Physics

04.11.2022

first assessor: Prof. Thomas Klinger
second assessor: Prof. Peter Manz

supervisor: Dr. Felix Reimold
thanks to: T. Romba, G. Partesotti

Contents

1 Introduction

1.1 Methods of transforming and storing Energy

Life depends on the ability to convert energy to locally decrease entropy [1]. Kinetic potential and chemical energy is stored and converted in the form of hunting by projectile acceleration, movement by building and releasing muscle tension, and many more. ATP is produced by oxidative phosphorylation via the energy from oxidation and subsequently used to drive processes in living cells.

Through technical development, humans are now able to exploit the thermal storage capability of steam, electrical batteries, fuel oxidation and fission, with fusion energy seemingly in reach. Fuel energy densities increased from around 10 MJ/kg when burning coal [2] to over 10^8 MJ/kg for $^{235}_{92}$U (Uranium-235) fission and deuterium-tritium $^{2}_{1}$H, $^{3}_{1}$H fusion [3]. Current approaches for fission and fusion both lead to nuclear waste, but for fusion reactors, waste would reduce to only the reactor itself and stop radiating significantly in a few hundred years [3], circumventing permanent underground storage. With the rising energy needs of humanity, this incentivizes research in harnessing fusion reactions for energy production.

The binding energy gives the energy needed to separate a nucleus into its nucleons. Every fission and fusion reaction converts a number of nuclei into other nuclei. However, the sum of resultant binding energies differs from the sum of the reactant binding energies. If the binding energy sum increases during the reaction, more energy will be needed to separate each nucleon, so under conservation of total energy, it has to be released by the reaction, normally in the form of electromagnetic radiation or kinetic energy of the products. As such, energy outputs from fission and fusion can be understood via the binding energy difference of the products and reactants. Figure 1 shows the averaged binding energy for some relevant nuclei. It decreases for big and small mass numbers, with a maximum average binding energy at and around ^{56}Fe and ^{62}Ni. For heavy nuclei, the average bind-

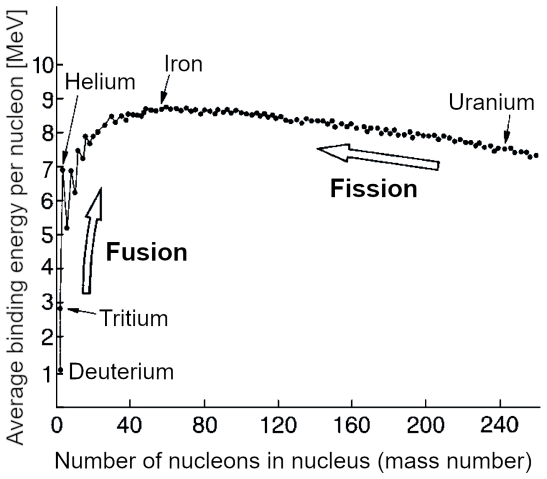

Figure 1: Average binding energy per nucleon plotted for different atomic nuclei. Taken from [3].

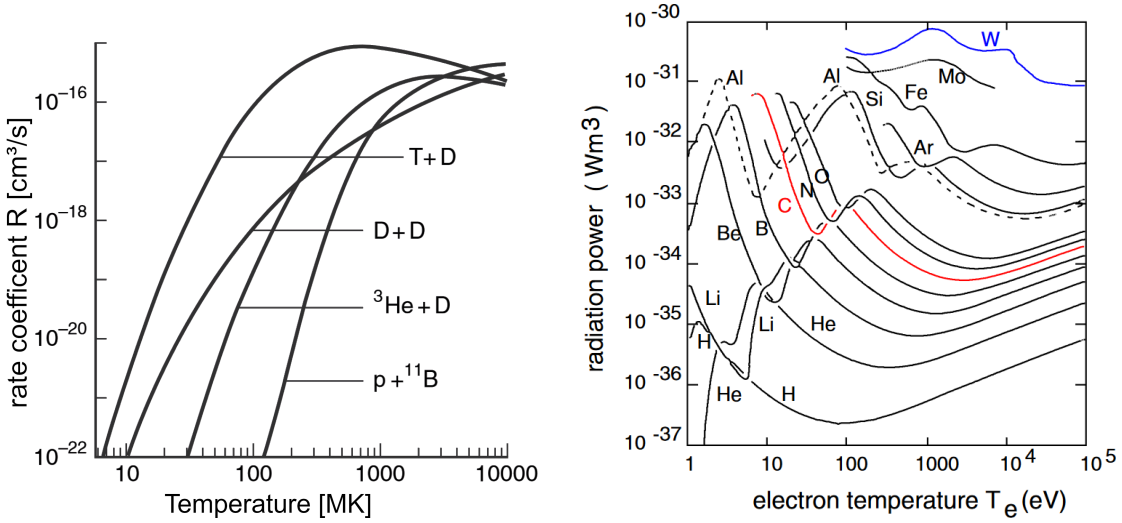

(a) fusion reaction rates, from [3]

(b) Impurity radiation, from [5]

Figure 2: Fusion reaction rates in a Maxwellian distributed plasma are dependent on temperature and type of reaction, which is shown in figure 2a. Inside the plasma, high-Z species radiate energy away, cooling the plasma (figure 2b). To maximize fusion output, the temperature needs to be optimized with both effects in mind. ($10\,\mathrm{MK} \mathrel{\widehat{=}} 860\,\mathrm{eV}$)

ing energy increases during fission into lighter nuclei, so more energy is needed to separate all nucleons after the reaction. The extra energy was released during the fission process. For nuclei in the mass range of iron, neither fusion nor fission can extract further energy. Massive stars have iron cores for this reason [4].

1.2 Fusion Energy Utilization

1.2.1 Optimized Fusion Conditions

To utilize energy from fusion, correct conditions for exothermic fusion reactions must be established. This is done by heating a confined ensemble region of the educt nuclei to high pressures and temperatures, creating a plasma. During their collision, the nuclei are now able to get close enough to have a significant probability of tunneling through the coulomb barrier of each other, thus fusing together.

In a thermalized plasma, the total fusion reaction rate R_{tot} depends on the densities ρ_1, ρ_2 of both nuclei, plasma volume, temperature and type of reaction, with the normalized rate R shown in figure 2a. Multiplying by released energy per reaction E_{fusion} then yields the total fusion power $P_{\mathrm{fusion}} = R_{\mathrm{tot}} E_{\mathrm{fusion}} = \rho_1 \rho_2 V R(T) E_{\mathrm{fusion}}$.

Multi-collision processes are possible, but the rates are insignificant at achievable pressures. For low temperatures, tunneling probabilities vanish. For high temperatures, with kinetic energies not negligible compared to the coulomb barriers, interactions between the nuclei decrease.

Types of reactions considered are:

$$\begin{aligned} {}^2\mathrm{D} + {}^2\mathrm{D} &\longrightarrow {}^3\mathrm{T}\,(1.0\,\mathrm{MeV}) + \mathrm{p}^+\,(3.2\,\mathrm{MeV}) \\ {}^2\mathrm{D} + {}^2\mathrm{D} &\longrightarrow {}^3\mathrm{He}\,(0.8\,\mathrm{MeV}) + \mathrm{n}\,(2.5\,\mathrm{MeV}) \end{aligned} \tag{1}$$

$${}^2\mathrm{D} + {}^3\mathrm{T} \longrightarrow {}^4\mathrm{He}\,(3.5\,\mathrm{MeV}) + \mathrm{n}\,(14.1\,\mathrm{MeV}) \tag{2}$$

$${}^2\mathrm{D} + {}^3\mathrm{He} \longrightarrow {}^4\mathrm{He}\,(3.6\,\mathrm{MeV}) + \mathrm{p}^+\,(14.7\,\mathrm{MeV}) \tag{3}$$

$$\mathrm{p}^+ + {}^{11}\mathrm{B} \longrightarrow 3\,{}^4\mathrm{He}\,(\Sigma\ 8.7\,\mathrm{MeV}) \tag{4}$$

Their rate coefficient is shown in figure 2a. Deuterium-tritium fusion is the most relevant reaction due to its high reaction rate at lower energies [6]. In confined plasmas, the uncharged neutrons exit the plasma with most of the energy, while reactions with charged products only would further heat the plasma. Non-fusing ions in the plasma are called impurities. For small enough atomic numbers, they may be fully ionized at fusion temperatures (low-Z impurities). Low-Z impurities, such as the fusion products, dilute the plasma, decreasing α-particle heating (see subsection 1.2.3) and converting some thermal energy to radiation via bremsstrahlung. High-Z impurities do not fully ionize in the fusion plasma, radiating energy via ionization and excitation processes as well [7]. At densities relevant for dilution, they would extinguish the plasma. As shown in figure 2b, radiative losses from high-Z impurity nuclei are much higher. For low-Z impurities, densities are high, especially for fusion products like helium, which significantly dilute the plasma. More detail about impurity radiation is given in section 3.3.

1.2.2 Magnetic Confinement Fusion and Stellarators

The fusion plasma needs to be confined to keep it at temperatures needed for fusion, because interacting with non-plasma materials would extinguish it. Either the timescales are small enough that physical distance to the environment in the vacuum suffices, or the plasma particle trajectories are bent via electromagnetic fields. In inertial confinement fusion (ICF), small volumes of high-density plasma are created, leading to a large number of fusion reactions before the plasma can reach the walls.

Penning traps are an example of the other approach, and confine plasmas radially with a uniform magnetic field created by a solenoid, and axially in an electric potential well.

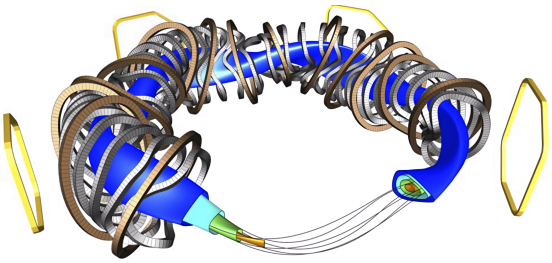

Figure 3: Cutaway diagram of the W7X coils and plasma. Non-planar coils in silver, planar coils in brown and trim coils in yellow. Taken from [8]

The plasma particles can only move along the magnetic field lines, coiling around them abiding by Lorentz's Law. To confine plasmas with magnetic fields only, called magnetic confinement fusion (MCF), a vacuum volume with magnetic field lines constrained to the inside of this volume needs to be created. This can be solved by bending the ends of the solenoid together so it forms a torus, like the brown coils in figure 3. Magnetic field lines inside the toroid form circles (toroidal direction), staying confined, with the plasma particles coiling around them (poloidal direction).

A naively constructed torus field would have lower magnetic flux densities on the outer than the inner field lines, leading to so-called ∇B-Drifts. In a section of higher magnetic flux density, the Lorentz force is larger, tightening the bend of the particle path around the field line. When moving along a field line perpendicular to a magnetic flux density gradient, the curvature increases on only one side, causing a vertical drift perpendicular to both B and ∇B, and opposite for electrons and ions [3]. Over time ions and electrons separate vertically, creating an electric field. The electric field in turn leads to higher velocities and greater radii of curvature in electrical force direction and a $\vec{E}$-drift perpendicular to B and E, annihilating the plasma by wall interactions. If the magnetic field lines loop poloidally as well, the vertical drift effects along a magnetic field line cancel out and emergent drifts are suppressed.

A poloidal component of the field lines can be generated by inducing a toroidal current into the plasma via ramping poloidal field coils. Such an approach is used by tokamaks. However, analogous to a transformer, the plasma current is proportional to the derivative of the poloidal field coil current. To maintain a constant plasma current, the coil current would need to increase indefinitely. Alternatively, a poloidal field component can be introduced directly by adding helical coils of alternating current direction around the torus [6]. At each crossing of a helical and toroidal field coil, the coils can technically be rewired so the outgoing wires are switched, introducing bends into the resulting coils. This procedure can be used to eliminate toroidally wrapping coils, ending up at the silver coils in figure 3 for the case of W7X.

1.2.3 The Lawson Criterion and the triple Product

A fusion plasma is heated to fusion temperatures externally. After starting to fuse, it (partially) heats itself (P_α) via the charged fusion products like α-particles in the case of D-T fusion. Some of the total energy is lost to the environment via impurity radiation or transport of energetic particles.

$$P_{\text{heat, external}} + P_\alpha = P_{\text{loss}} \qquad (5)$$

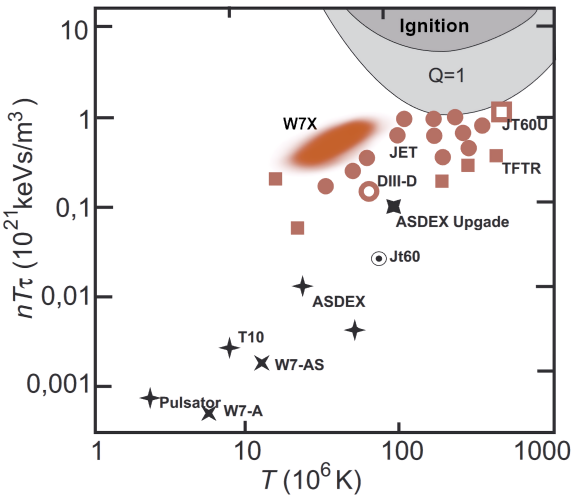

Figure 4: Achieved triple products. Taken from [6], edited with data from [3]

Terms for α-particle heating and energy losses assuming constant plasma temperature and density are derived in [9, 6]. In the case of plasma ignition, α-particle heating suffices to keep the plasma at fusion temperatures, and no external heating is needed. Including this into equation 5 yields an inequality necessary for a burning plasma, the Lawson burn criterion:

$$0 \overset{!}{\geqslant} \frac{P_{\text{heat, external}}}{V} = \frac{3n_iT}{\tau_E} - \frac{\Delta E_i n_i^2 R(T)}{4} \quad \Longrightarrow \quad n_iT\tau_E \geqslant \frac{12}{\Delta E_i}\frac{T^2}{R(T)}\,, \qquad (6)$$

using the averaged ion number density n_i, temperature T, fusion reaction rate R, kinetic energy ΔE_i of the charged fusion products (α-particle) of a single reaction and energy confinement time $\tau_E = E_{\text{plasma}}/P_{\text{loss}}$ [6, 10]. The triple product $n_iT\tau_E$ is shown for some experiment runs in figure 4 plotted against temperature, with higher values getting closer to an ignited plasma. With impurities diluting the plasma, α-particle heating at impurity density n_z reduces to $P_{\alpha,n_z} = P_\alpha \cdot (1 - Zn_z/n_i)^2$ due to the dilution of both deuterium and tritium in the plasma [10]. Defining the fusion energy gain factor Q as the ratio of total fusion energy to external heating energy, Q will go to infinity for an ignited plasma. For an economical fusion reactor, Q needs to be much greater than 1, so electricity used for heating the plasma can be compensated by electricity generated from the excess heat. ITER aims to reach $Q = 10$ [6]. For comparable temperatures, higher fusion products equate to higher gain factors, being good estimators of fusion capabilities in MCF.

1.2.4 W7X Magnetic Field

In general, the closed magnetic field lines in W7X do not reconnect with themselves after a finite number of toroidal rotations, but they will get arbitrarily close again. The (approximated) ratio of poloidal rotations to toroidal rotations is called the rotational transform ι, defined locally via the poloidal and toroidal fluxes [11, 6].

$$\iota := \frac{\mathrm{d}\psi_\theta}{\mathrm{d}\psi_\phi} = \frac{\text{Number of poloidal turns}}{\text{Number of toroidal turns}} \approx \frac{RB_\theta}{rB_\phi}$$

For irrational ι, field lines have infinite length and form a surface, called magnetic flux surface. The surfaces are nested inside each other like layers of a toroidal onion. The most central surface is called the magnetic axis. At rational ι surfaces, magnetic islands (flux surfaces not containing the magnetic axis) can form from disturbance field interactions. W7X intentionally introduces disturbance fields for the 5/5 island chain. The main islands of W7X are shown in figure 9 and 10, with higher order islands in [12].

1.2.5 Power Exhaust and Divertor

In fusion reactors, plasma heat is conducted outwards and must be removed, so the vessel does not overheat. A last closed flux surface exists, outside of which the innermost part of the wall (limiter) is intersected by the adjacent flux surface. Because the heat conductivity in toroidal and poloidal direction is much larger than between flux surfaces [14], most of the heat flow into the adjacent flux surfaces is consequently dissipated into the limiter intersecting it, instead of being conducted further outwards. The energetic particles carrying the heat collide with the limiter, sputtering impurities back to the plasma core, increasing radiation losses and cooling the plasma. With heat flow on the order of MW, power densities on the limiter much higher than achievable cooling rates would melt it. Thus, W7X uses a 5/5 island chain with targets outside the inner separatrix (divertors). Around the separatrix, $\iota \approx 1$, and the iota relative to the island goes to zero. Therefore, connection lengths to the target increase and more heat can be conducted to neighboring

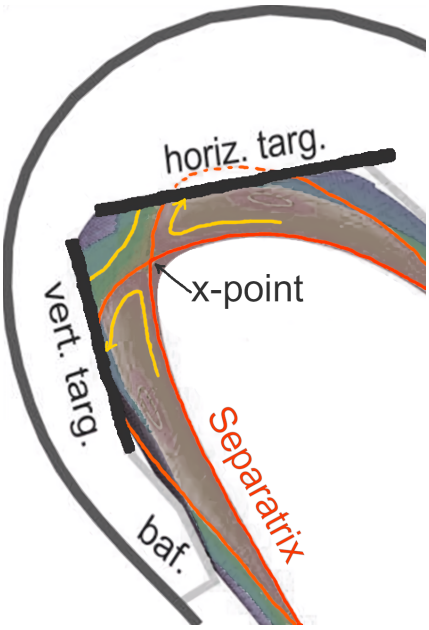

Figure 5: W7X Divertor. Taken from [13] and edited.

flux surfaces, spreading out the power dissipated on the divertor. With islands, impurities are kept outside of the core plasma and stay close to the targets. There, the energetic plasma particles can transfer energy to the impurities, which gets radiated away isotropically, reducing power densities on the targets even further to manageable levels of a few $\mathrm{MW/m^2}$ [15]. The reduction of heat load via impurity radiation is called detachment [13].

2 EMC3-Eirene

2.1 Modeling the Edge Plasma Behaviour

In the edge region, plasma interactions with other particles need to be considered. This includes neutral hydrogen gas and atoms, and ions and atoms of all other species injected and sputtered by the plasma. The non-hydrogen species in the plasma are impurities, and together with the neutral hydrogen need to be modeled when simulating an edge plasma.

> "EMC3 is a 3D fluid code for both the background plasma and impurities and solves the [Braginskii] fluid equations by applying a Monte Carlo method on a locally field-aligned vector basis. EIRENE is a 3D kinetic Monte Carlo Code for neutral particles, [and while not used in W7X], radiation transfer and kinetic trace ion impurity transport." ([16])

2.1.1 Plasma Transport Model

Microscopically, a plasma is described as an ensemble of electrons and ions, each with a mass, charge position, and velocity vector. Particles interact with each other and the external electromagnetic field, describing the plasma via their collective behavior. The information about all particles of one species S can be specified as a distribution function $f_S(t, \vec{r}, \vec{v})$, which gives the density of particles from that species at each position and velocity. The behavior of the plasma is then described by integration of the Boltzmann equations (7), a system of kinetic equations relating each distribution function [17, 18].

$$\underbrace{\frac{\partial f_\alpha}{\partial t}}_{\text{(i)}} + \underbrace{\sum_\beta \frac{\partial}{\partial x_\beta}\left(v_\beta f_\alpha\right)}_{\text{(ii)}} + \underbrace{\sum_\beta \frac{\partial}{\partial v_\beta}\left(\frac{F_{\alpha\beta}}{m_\alpha} f_\alpha\right)}_{\text{(iii)}} = \frac{\partial f_\alpha}{\partial t} + \vec{v}\cdot\boldsymbol{\nabla} f_\alpha + \frac{\vec{F_\alpha}}{m_\alpha}\frac{\partial f_\alpha}{\partial \vec{v}} = C_\alpha \quad (7)$$

$$\text{with} \qquad \vec{F}_{\alpha,\text{all}} = Z_\alpha e \cdot \left(\vec{E} + \vec{v} \times \vec{B}\right)$$

Here α specifies the species concerned, and β the components of the position and velocity vector $\vec{x}, \vec{v}$. The change in the density distribution (i) at some position happens as a consequence of diffusion (ii) to or from that position and force-induced movement of the particles. This force-induced movement is split into a macroscopic force-induced movement (iii) from the global field as well as macroscopic charge density differences, and into the collision term C_α that arises from the microscopic particle-particle interactions of the species with itself and every other species. The macroscopic Lorentz force $\vec{F}_\alpha$ is defined such that it does not take small-scale changes in $\vec{E}$ and $\vec{B}$ into account, which leaves C_α as an extra term.

Now taking zeroth, first and second-order moments of velocity of the kinetic equations yields three new equations. When simplified using the definitions of "mean temperature" T_α, "mean velocity" $\vec{u}_\alpha$ and "particle density" n_α,

$$n_\alpha = \int \rho_\alpha \,\mathrm{d}\vec{v} \qquad \vec{u}_\alpha = \frac{1}{n_\alpha} \int \vec{v} f_\alpha \,\mathrm{d}\vec{v} \qquad T_\alpha = \frac{1}{n_\alpha} \int \frac{m_\alpha}{3} \big(\vec{v} - \vec{u}_\alpha\big)^2 f_\alpha \,\mathrm{d}\vec{v}\,, \tag{8}$$

they reduce to differential transport equations describing the behavior of those quantities. They contain collision term integrals and higher-order velocity terms, which are not described by the equations themselves and must be closed in some other way, before the equations can be solved for $n_\alpha(t)$, $\vec{u}_\alpha(t)$ and $T_\alpha(t)$. Assuming small distribution gradients and thus velocity relaxation to a near Maxwellian distribution allows ad hoc closures to the transport equations [19, 18], yielding the Braginskii equations. For use in EMC3, further simplifications (like ignoring parallel diffusion due to much larger parallel transport) were made [20]. These resulted in equations (9,10,11), governing particle transport (9), momentum transport (10) and energy transport (11) shown for a model plasma with H^+ as the only ion species [18, 21, 22]. In that specific case n_e is equal to n_i, otherwise $n_e = \sum_\alpha n_{i\alpha} Z_\alpha$. The heat conductivity and heat diffusivity κ, χ, fluid viscosity η and diffusion coefficient D in radial, poloidal and toroidal direction are transport parameters with values either motivated by other models or to be chosen when running a simulation ($\chi_i, \chi_e, D_\perp = D_\mathrm{rad} = D_\mathrm{pol}$).

$$\boldsymbol{\nabla} \cdot \left[n_i \vec{u}_{i\parallel} \mathbf{e}_\parallel - D_\perp \mathrm{I}_\perp \boldsymbol{\nabla} n_i \right] = S_p \tag{9}$$

$$\begin{aligned} \boldsymbol{\nabla}_\parallel \cdot \left[m_i n_i \vec{u}_{i\parallel}^2 - \eta \mathbf{e}_\parallel \boldsymbol{\nabla} \vec{u}_{i\parallel} \right] - \boldsymbol{\nabla}_\perp \cdot D_\perp \boldsymbol{\nabla} \big(m_i n_i \vec{u}_{i\parallel} \big) \\ = S_m - \mathbf{e}_\parallel \cdot \boldsymbol{\nabla} (n_e T_e + n_i T_i) \end{aligned} \tag{10}$$

$$\begin{aligned}\boldsymbol{\nabla}_\parallel \cdot \left[\frac{5}{2} T_e n_i \vec{u}_{i\parallel} - \kappa_e \mathbf{e}_\parallel \boldsymbol{\nabla} T_e\right] - \boldsymbol{\nabla}_\perp \cdot \left[\chi_e n_i \boldsymbol{\nabla} T_e + \frac{5}{2} T_e D_\perp \boldsymbol{\nabla} n_i\right] \\ = S_{ee} - \frac{3 m_e}{m_i} \frac{n_e}{\tau_{ei}} (T_e - T_i) - \mathcal{S}_{e,\mathrm{cool}} \\ \boldsymbol{\nabla}_\parallel \cdot \left[\frac{5}{2} T_i n_i \vec{u}_{i\parallel} - \kappa_i \mathbf{e}_\parallel \boldsymbol{\nabla} T_i\right] - \boldsymbol{\nabla}_\perp \cdot \left[\chi_i n_i \boldsymbol{\nabla} T_i + \frac{5}{2} T_i D_\perp \boldsymbol{\nabla} n_i\right] \\ = S_{ei} + \frac{3 m_e}{m_i} \frac{n_e}{\tau_{ei}} (T_e - T_i)\end{aligned} \tag{11}$$

They are Fokker-Planck equations describing the evolution of their macroscopic quantities driven by their distribution and possible sources or sinks on the right-hand side: effects due to plasma neutral interactions (S_p, S_m, S_{ee}, S_{ei}), electron-ion temperature coupling and a pressure drive in the momentum equation. $\mathcal{S}_{e,\mathrm{cool}}$ describes the main contribution of impurity ions; their cooling effect is due to radiation, which is described in the impurity model.

2.1.2 Impurity Model

The impurity model needs to solve the same three quantities $n_\alpha(t)$, $\vec{u}_\alpha(t)$ and $T_\alpha(t)$, for each impurity ion, but simplifications to the equations of the different moments are made [14, 22].

The particle transport equation contains parallel transport and diffusion in both the parallel, as well as the perpendicular direction. Ionization and recombination are included as source terms and calculated from atomic data (see section 2.1.3).

The momentum balance is modeled as the force balance for the impurities due to thermal and pressure gradients and differences between ion and impurity velocity. This provides the velocity for the parallel convection term $\vec{u}_{Z\parallel}$ in the particle balance. The impurity temperature is set to be equal to the plasma ion temperature $T_i = T_{Z,\mathrm{imp}}$ as a further simplification. Impurity concentrations are assumed to be small and are handled in the trace approximation with no effect on the main plasma model, with the exception of heat losses due to radiation. So the impurities need not be taken into account for the approximate behavior of the plasma, with the exception of radiation.

2.1.3 Neutral Model & Eirene

Neutral particles get simulated kinetically by EMC3/Eirene. In each iteration, the macroscopic plasma and impurity quantities get calculated and neutral particle

ensemble movement is simulated by EMC3. Afterward, the local macroscopic quantities are given to Eirene.

Eirene is a neutral transport code with a large database of atomic data. It solves the kinetic Boltzmann equation for neutrals, taking into account plasma-neutral interactions and plasma surface interactions like particle and energy reflection or impurity sputtering. The results of those calculations then inform the next iteration of the EMC3 simulation as they provide the source terms used in the plasma and impurity models. The whole model eventually reaches a steady state whose quality in modeling a physical plasma depends on the specific approximations made in the code as stated above, as well as the quality of the grid given on which the code operates. A full description of the Eirene capabilities is given in [23, 24].

Both EMC3 and Eirene are implemented as Monte-Carlo codes solving their specific Fokker-Planck equation numerically using the equivalence to a stochastic process [21, 25].

2.2 Grid Generation and Optimization

EMC3 calculates its macroscopic quantities on a domain of 3D space numerically. For the numerical simulation, the domain needs to be discretized, which is done by generating a grid containing the inside of the plasma vessel. Drifts are ignored, so magnetic field magnitude has no effect on plasma tracing. The grid used in EMC3 is field-aligned (inside the separatrix) and contains the direction of the magnetic field along its field-aligned axis inside the plasma region. A simple grid for the W7X structure is shown in figure 6. Due to the magnetic field topology of tokamaks and stellarators, and EMC3 requirements, a mapping from a 3d interval into a toroidal space is used as a grid by evaluating the mapping at the grid vertices. In the simplest case, the grid mapping is a perfect torus:

$$\begin{array}{rccl} g_R\colon [r_1, r_2] \times [0, 2\pi] \times [0, 2\pi] & \to & \mathbb{R}^3 \\ (\, r \quad , \quad \theta \quad , \quad \varphi\,) & \mapsto & \big((R + r\cos\theta)\cos\varphi,\ (R + r\cos\theta)\sin\varphi,\ r\sin\theta\big), \end{array}$$

or for discretely mapping the vertices directly,

$$g_R\colon \{1, \ldots, N_r\} \times \{1, \ldots, N_\theta\} \times \{1, \ldots, N_\phi\} \quad \longrightarrow \quad \mathbb{R}^3.$$

For W7X, the deformations of the torus shape need to be considered as well.

Notice that the toroidal grid structure leads to a hole inside the toroidal structure, (or a singularity at the toroidal center axis if $r_1 = 0$). This is fine as EMC3 is not concerned with modeling the plasma core. The continuous mappings can generate ever-finer grids that show superior numerical accuracy to subdivision of grid cells if g_R is smooth [26].

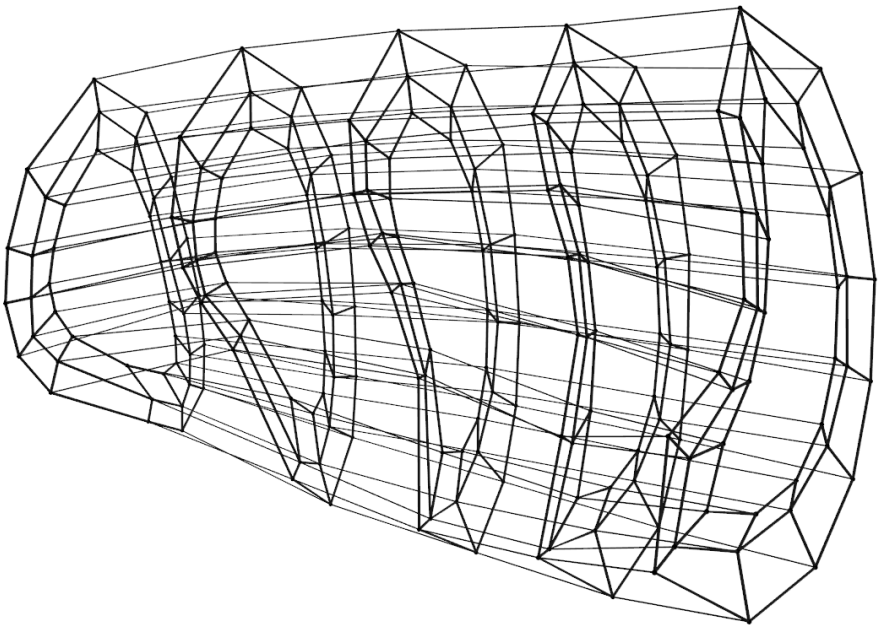

Figure 6: Minimal toroidal field line traced W7X grid, unwrapped toroidally.

Nonetheless, numerical characteristics of the discrete grids need to be quantified to give accuracy estimates on the results obtained by simulating plasmas on them. With gradient calculations depending on the shape of the grid cells, grid cell measures like skewness, non-orthogonality, and unevenness given in [26] can be defined and investigated for effects on accuracy.

They were found to have an impact on gradient calculations by Jacobs as part of his thesis work [27].

Furthermore, the EMC3 grid requires convex cells to allow for a unique bilinear interpolation along the field line. A grid generator for the W7X structure was developed and extended by various routines in this work to optimize the generated grids for convexity and the grid quality measures given. The intent is to provide a grid generation tool that allows generating grids needed for nonstandard magnetic configurations and full torus simulations ($\Delta\phi = 360°$). This makes studying toroidal and radial asymmetries due to localized puffs or error fields possible.

2.2.1 Half-module Optimization via Grid Quality Measures

To accurately simulate the plasma, the EMC3 grid needs to be field line traced inside the region of closed flux surfaces (inner cell ring in figure 6). In the neutral region with diverging field lines, grid cells must be mapped by some other way to

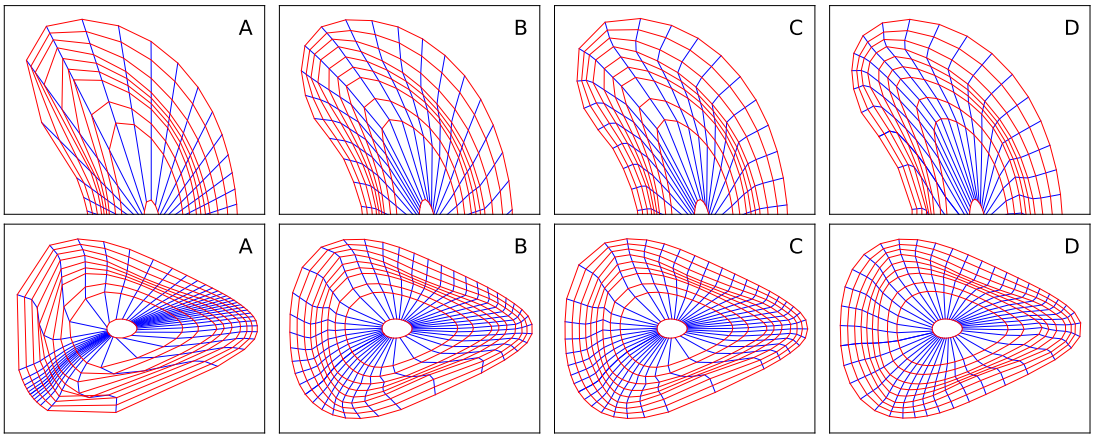

Figure 7: Optimized subsampled grid cross sections: naïve radial projection (A), equal spaced points on inner flux surfaces and density function distributed points on the vessel (B), equal spaced points on inner flux surfaces and surface normal vessel projection (C), optimized tracing starting angle, grid line Zoidberg smoothing and optimization in C (D).

cover the space to the plasma vessel surface (outer cell ring in figure 6). Multiple approaches have been considered and implemented, shown together with the effort of minimizing the grid distortion inside the closed flux surface in figure 7.

Naïvely projecting outwards from the magnetic axis leads to problems with grid convexity at the bean cross section (top row in figure 6), and large cell density distortions after tracing the projected cross-section to other toroidal angles. To combat this, the grid vertices poloidally along a flux surface at the starting cross section can be spaced equally. Equal vertex spacing along the plasma vessel is difficult, as the vessel shape differs significantly from the flux surface shapes, again leading to concave or overlapping cells along bends. This can be addressed by manually defining a vertex density distribution over the vessel surface, like in figure 7b.

Another approach to generating the Grid between the last closed flux surface and the vessel surface can be taken by calculating the surface normal of each grid vertex and interpolating the grid via the projection along the normal vector to the intersection with the vessel. Concave surfaces can lead to an overlap of such normal projections. However, by nearest-neighbor smoothing the normal vectors, the distribution of the vessel vertices increases in uniformity as the normal vectors get more parallel, which has the effect of undoing such overlaps. See figure 7c.

Finally, the cross-section to start the field line tracing can be varied, as can the

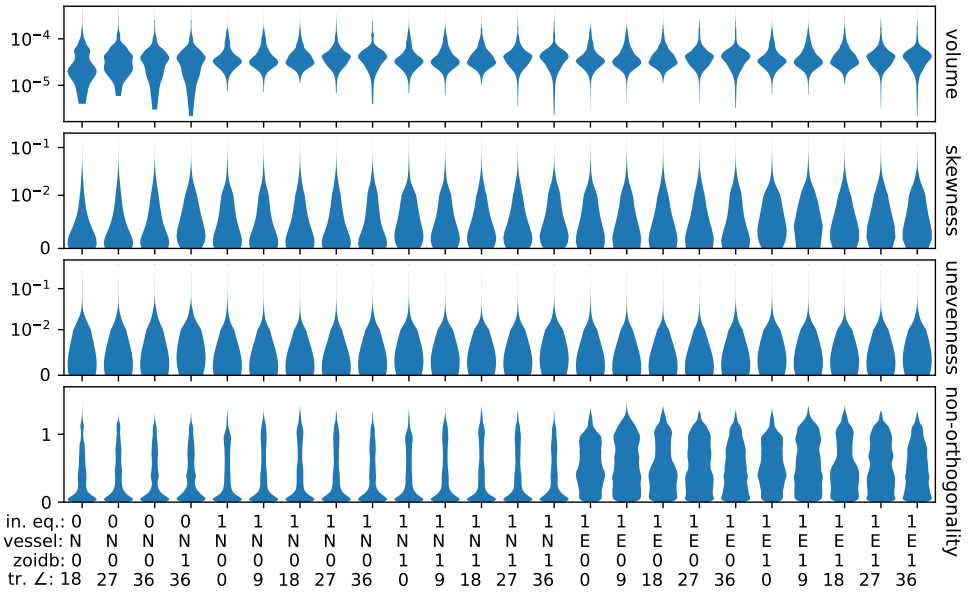

Figure 8: Grid quality measure plot to investigate the effects of the implemented grid optimization routines for all convex testing grids generated. Shown in the rows are the distributions of the volume and grid measures as defined in [26] over all of the cells of the grid. Each column is associated with one grid, generated by the parameters specified in the labels.

interpolation vertices between to fitted flux surfaces at the starting cross-sections to try to soften kinks in the iso-radial and iso-poloidal grid lines, as shown in figure 7D. Tracing forward and backward toroidally from the middle of the module has a large effect, as cell distortion inside the closed flux surfaces inevitably increases along the field line because their distances and angles change from the optimized shape at the starting surface.

The effects of those optimization routines can now be quantified by calculating the convexity, volume, and grid measures for each cell of a grid, which is depicted for every convex grid in figure 8, with all grids shown in the appendix (figure 36). A grid can have equally spaced vertices on the flux surfaces (in.eq. = 1), and the grid lines can be smoothed by the Zoidberg algorithm (zoidb. = 1). Furthermore, the angle $\alpha \in [0°, 36°]$ of the tracing surface can be varied over the whole half module (tr. $\angle = \alpha$). Lastly, the projection type from the last closed flux surface to the vessel surface was also varied over radial projection (P), normal projection (N), equal vessel spacing (e), and vessel spacing via a density function (E). The last projection is not given for each parameter combination and is also less relevant for the quantification due to being manually defined, but is still given as a rough

estimation of what to expect from such an approach.

A good grid would be convex, have small grid quality measures, and uniformly sized cells. In the set of tested grids, every grid generated from equal vessel spacing and radial projection is not convex for the reasons given before. Ignoring those, convex grids can predictably be generated by ensuring no such cells via the density function defined vessel spacing, but with drastically higher non-orthogonality than the surface normal projection while not improving any other measure.

Equal flux surface vertex spacing decreases unevenness and satisfies convexity to the cost of skewness. Extreme tracing surface angle values lead to more uneven grids while tracing angles closer to the triangular cross-section have better cell volume distributions, seemingly because the cell distortion in the bean shape coincides with the large poloidal radius distortion at the right poloidal angles, partially canceling the effects. Using the Zoidberg smoothing worsens the grid's unevenness and skewness, if only slightly, but offers no advantages and is therefore not considered further.

2.2.2 Stochastic Flux Surfaces

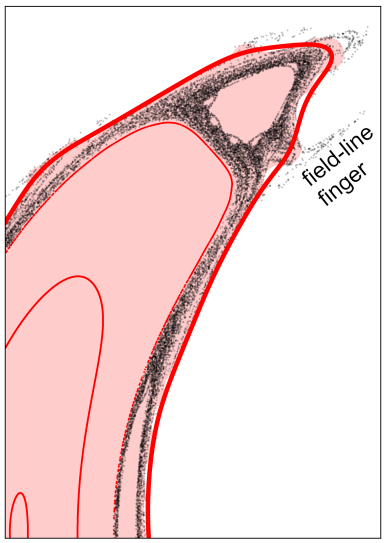

Figure 9: Chaotic FTM poincaré map and solution to surface creation problem.

To define Flux surfaces, Poincaré maps of a simulated particle traced along the magnetic field lines are used. In practice, this works well inside of the separatrix at $\iota < 1$, as shown by the inner three red surface cross sections in figure 9. Outside of it, the resonant modes at rational ι and specifically the dominant one for the configuration keeps the flux surfaces from surrounding the magnetic axis until another range of ι without simple rational values is reached, where closed flux surfaces either reoccur, or the magnetic field stops being toroidal and field lines become open ended[1]. Between these two regions, a stochastic region may exist caused by the interaction of island chains fulfilling the Chirikov criterion [28], as shown by the black markers in figure 9. The local behavior

[1]The field lines themselves are always closed. In magnetic confinement, however, field lines heading outside of the plasma volume are considered open as the path of a particle following the field line ends at the vessel surface.

is still well-defined as all particles follow the magnetic field which changes slowly in space. But a traced particle stops to generate a surface. Instead, it varies inside of a volume. In the shown FTM grid, no closed flux surface exists outside of the stochastic region, but an outer surface surrounding the islands is still required to simulate the plasma correctly within EMC3. It does not need to be a flux surface as long as it surrounds the islands and stays inside the field line traceable region to extend it to other cross-sections for the grid generation. Such a surface was generated by generating an alpha shape, eroding it by removing parts of the shape close to the surface and adding parts close to the shape surface back in, resulting in removing the fingers spreading outwards, and smoothing the resulting shape to get rid of high-frequency oscillations complicating the grid-vessel extension.

2.2.3 Flux Surface Asymmetry from Magnetic Fields

When investigating plasma behavior without a toroidally periodic and symmetric magnetic field, e.g. to examine the effects of combined islands shown in figure 10, field line tracing in the first half module only is not enough to generate a grid applicable to the whole torus. Due to a change in iota of 0.1 to 0.3 radially outwards [29], after one Orbit the outer flux surfaces will be twisted against the magnetic axis by the iota difference as a fraction of a turn. More importantly, the islands also rotate, so two radially ordered (with respect to the main magnetic axis) points on the same island switch their order when traced for a long enough distance. As vertices in EMC3 grids keep their radial and poloidal parameterization when traced toroidally, this invalidates grids with a large toroidal extent. Because of that, field line tracing over the whole torus is also not applicable to the magnetic fields used. Instead, each module is traced independently of the other grids and the grids are stitched together via mapping surfaces which would be needed in all approaches to map the 360° cross-section back to the first one at 0°.

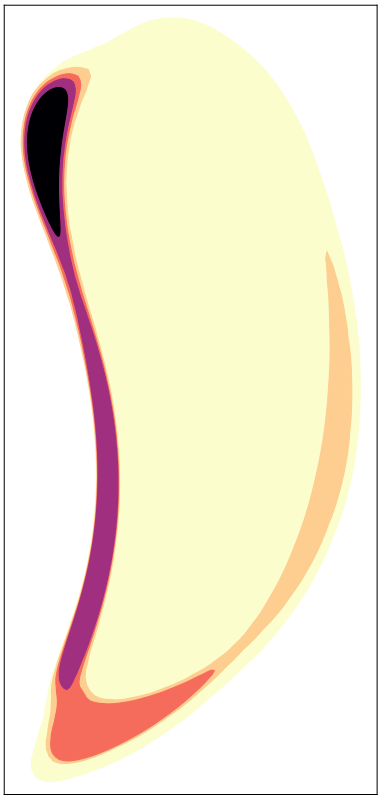

Figure 10: Island structure on perturbed EIM field on 13° (QRB) cross-section.

3 Radiation

3.1 Plasma Radiation Sources

Radiation is the consequence of photon emission from plasma particles due to a number of effects. The most important ones are bremsstrahlung and line radiation from deexcitation and recombination.

Bremsstrahlung In high-temperature plasmas, energies of the charged plasma particles are high, facilitating collisions with small minimum particle distances. During these collisions, both particles emit bremsstrahlung. However, only the collisions between particles of different specific charge (q/m) emit dipole radiation, with higher order radiation from particles of the same specific charge being insignificant [30, 31]. In the W7X hydrogen plasma with impurities, this leaves $(\mathrm{e}^-, \mathrm{p}^+)$, $(\mathrm{e}^-, \mathrm{X}_{\mathrm{imp}})$, $(\mathrm{p}^+, \mathrm{X}_{\mathrm{imp}})$ and $(\mathrm{Y}_{\mathrm{imp}}, \mathrm{X}_{\mathrm{imp}})$ collisions. The amount of bremsstrahlung scales with the sum of the specific charges [31], so $(\mathrm{e}^-, \mathrm{p}^+)$ collisions decrease in importance in areas of high impurity concentrations like the plasma edge. Bremsstrahlung is relevant at high n_e, T_e in a future reactor, but less so in present-day devices.

Recombination Radiation As a significant fraction of the atoms in a plasma are ionized, recombination can occur, if only for a short time before reionization. The energy of the continuum electron that recombines is partially radiated directly as a photon, with the rest remaining in the form of an excited state.

Deexcitation Radiation Ions are excited by electron impact collisions after a recombination event. These exited ions undergo deexcitation into less energetic states over time and emit a line radiation photon in the process. No excited state exists for fully ionized particles, so they only emit bremsstrahlung. At densities of $10^{20}/\mathrm{m}^3$, for temperatures above 2 eV, less than 1‰ of the hydrogen atoms in the plasma are not ionized in steady state isotropic (no transport) conditions. Below 2 eV, the excitation cross sections diminish. Carbon impurities stay only partially ionized up to hundreds of eV (figure 11). Thus, plasma deexcitation radiation is dominated by impurity radiation

Synchrotron Radiation Besides collision acceleration, electrons and ions in a magnetic field get accelerated via the Lorentz force on their helical paths along the magnetic field, emitting synchrotron radiation. Synchrotron radiation scales

strongly with increasing speed, and therefore decreasing mass, so only electrons need to be considered. With plasma core temperatures below 10 keV, only a minuscule fraction of the electrons reach relativistic speed, so the radiation can be calculated roughly with some approximations in the non-relativistic cyclotron limit.

$$\begin{aligned} P_{\mathrm{cycl},\,e} &= \frac{\sigma_e B^2 v_e^2}{c\mu_0} = \frac{2\sigma_e B^2 T_e}{c m_e \mu_0} \approx 8 \cdot 10^{-16}\,\mathrm{W} \\ P_{\mathrm{cycl,\,tot}} &= P_{\mathrm{cycl},\,e} \cdot n_e V \approx 1\,\mathrm{MW} \end{aligned} \tag{12}$$

where the Thomson cross section σ_e of the electron, the speed of light c and the vacuum permeability μ_0 are physical constants and $B = 2.5\,\mathrm{T}$, $V = 30\,\mathrm{m}^3$, $n_e = 4 \cdot 10^{19}/\mathrm{cm}^3$ and $T_e = 2\,\mathrm{keV}$ are chosen as rough averaged representative values for W7X during operation. Most of this radiation is absorbed again via photon absorption of surrounding electrons. However, the residual radiation can still lead to considerable losses, e.g. in ITER [32, 33].

In W7X, hydrogen plasma is used and no fusion takes place, so nuclear deexcitation radiation can be ignored. In the case of CRM models for W7X introduced below, recombination and bremsstrahlung of H^+ are not taken into account. In EMC3 simulations, a Maxwellian energy distribution of the free electrons is assumed, determined from the simulated electron temperature. This is then used to model radiation from excitation. Finally, for the synthetic bolometer measurements for whom the radiation data will be used later on, nuclear deexcitation and microwave synchrotron radiation can always be ignored, because high-frequency gamma radiation transmits through the bolometer [34], while microwave radiation gets shielded by a mesh in front of the bolometer [35]. For synthetic W7X bolometer measurements, bremsstrahlung, recombination and line radiation of impurity ions interacting with electrons modeled in EMC3 is thus even sufficient for plasmas with relevant amounts of fusion.

3.2 Adas

The rate of these reactions for the impurities and therefore the power that they radiate depends linearly on the plasma volume V and density n_e, n^z_{imp} of both the electrons and the impurity ions. For each reaction, the radiated power then depends on the reaction rate and transition energy, with the total radiated power as the total of each excitation and ionization transition plus bremsstrahlung. The population distribution along the excitation states is equilibrating on timescales faster than transport processes and hence assumed to be in an electron temperature and density-defined equilibrium. Effects of long-lived metastable excitation states

in delaying the equilibration process are ignored in this work. The radiated power can then be described by excitation state independent radiation power coefficients R^z only. Without any transport, the population distribution would equilibrate over ionization states as well giving a total radiative power, dependent only on electron temperature and density (shown density normalized in figure 13 as L_{tot}).

$$\frac{\mathrm{d}E_{\text{rad}}}{\mathrm{d}t} = P_{\text{rad}} = \sum_z V n_e n^z_{\text{imp}} \cdot \left(R^z_{\text{transition}}(n_e, T_e) + R^z_{\text{bremsstrahlung}}(n_e, T_e) \right) \tag{13}$$

To obtain the radiation power coefficients, the ADAS database[2] is used.

> "The Atomic Data and Analysis Structure (ADAS) is an interconnected set of computer codes and data collections for modeling the radiating properties of ions and atoms in plasmas. It can address plasmas ranging from the interstellar medium through the solar atmosphere and laboratory thermonuclear fusion devices to technological plasmas. " ([36])

The ADAS iso-nuclear master files provide a metastable unresolved set of coefficients.

$$\begin{aligned} R^z_{\text{line rad.}} &= \text{PLT}^z && \text{for line radiation driven by excitation and} \\ R^{z+1}_{\text{recomb.}} + R^{z+1}_{\text{bremsstr.}} &= \text{PRB}^z && \text{for recombination radiation and bremsstrahlung.} \end{aligned}$$

$$P_{\text{rad}} = V n_e \sum_{z=0}^{Z_{\text{imp}}-1} n^z_{\text{imp}} \, \text{PLT}^z(n_e, T_e) + n^{z+1}_{\text{imp}} \, \text{PRB}^z(n_e, T_e) \tag{14}$$

with PRB^z indicating the recombination from X^{z+1} to X^z as well as the bremsstrahlung of X^{z+1}. Thus, $\text{PRB}^z, \text{PLT}^z$ are defined for $0 \leqslant z < Z_{\text{imp}}$, where Z_{imp} is indicating the highest ionization level of the impurity.

The ADAS database also contains the effective rates for ionization and recombination of hydrogen and impurities. With this data, the evolution of the impurity species in terms of charge state given the plasma parameters of T_e, n_e, and neutral hydrogen density n_H for the impurity hydrogen charge exchange can be simulated.

$$\begin{aligned} &\text{SCD}^z && \text{for ionization from } X^z \text{ to } X^{z+1} \\ &\text{ACD}^z && \text{for recombination from } X^{z+1} \text{ to } X^z \\ &\text{CCD}^z && \text{for charge exchange: } X^{z+1} + \text{H} \longrightarrow X^z + \text{p}^+ \end{aligned}$$

[2] `https://open.adas.ac.uk/adf11`

3.3 Impurity Ionization Models

The radiation power coefficients are calculated by multiplying the effective rates for ionization and recombination with their transition energy and the density of the excited state. The effective rates and transition energies were found experimentally, and added to the ADAS database, but the density distribution must be calculated for the conditions found in the plasma by impurity ionization models.

3.3.1 Coronal and Collisional-Radiative Model

For small enough electron and hydrogen densities, interactions with the impurity ions (as well as between impurity ions) happen on a larger time scale than the relaxation of an excited impurity ion to its ground state. In that case, electron impact collisions that excite or ionize the ion are considered with ground-state impurity ions only. The change in density of an ionization level can be described as

$$\begin{aligned}\frac{\mathrm{d}n^z_{\mathrm{imp}}}{\mathrm{d}t} = {} & n_e n^{z-1}_{\mathrm{imp}} \cdot \mathrm{SCD}^{z-1} + n_e n^{z+1}_{\mathrm{imp}} \cdot \mathrm{ACD}^{z} + n_H n^{z+1}_{\mathrm{imp}} \cdot \mathrm{CCD}^{z} \\ & - n_e n^{z}_{\mathrm{imp}} \cdot \mathrm{SCD}^{z} - n_e n^{z}_{\mathrm{imp}} \cdot \mathrm{ACD}^{z-1} \,.\end{aligned} \tag{15}$$

for the intermediate ionization stages and without ionization or recombination and charge exchange for both fully- and unionized impurities. When equilibrated $\partial n^z_{\mathrm{imp}}/\partial t = 0$ for all ionization stages. Using a constant electron and hydrogen density, the resulting system of linear first-order ODE can then be solved by providing one of the densities or solving for fractional abundance $f_z \coloneqq n^z_{\mathrm{imp}}/\sum_z n^z_{\mathrm{imp}}$ with $\sum_z f_z = 1$. In the model of EMC3, charge exchange (CCD) contributions are ignored.

At higher electron densities the above assumption of excitation from the ground-state only can not be held up, as electron impact excitations become more frequent. Excited states then interact in multi-excitation processes. This leads to notable changes in the population density of the ground state ions, as well as large densities of metastable excited states. The total fractional abundances inside one ionization state yield unresolved fractional abundances, shown in figure 11. Equivalently, the unresolved PLT^z is given by the sum of every normalized transition radiation power $f_X \cdot \mathrm{rate}_{X\to Y} \cdot \Delta E_{X\to Y}$ from an exited state X to a less excited state Y, both with an ionization level z. Finally, the unresolved PRB^z is given by the total of normalized transition radiation powers from ionization level $z+1$ to level z.

This approach to calculating the rate coefficients is called the Collisional-Radiative Model (CRM). It also allows modeling non-equilibrium conditions. Total state population by excitation and deexcitation, as well as ionization, state depopulation, and charge exchange and recombination from other states are in detailed

equilibrium in steady-state conditions. The simpler low-pressure limit with states excited from ground states only is called the Coronal Model (CM), because of its application in modeling the sun's low-pressure coronal plasma.

3.3.2 CRM-based zero-dimensional Transport

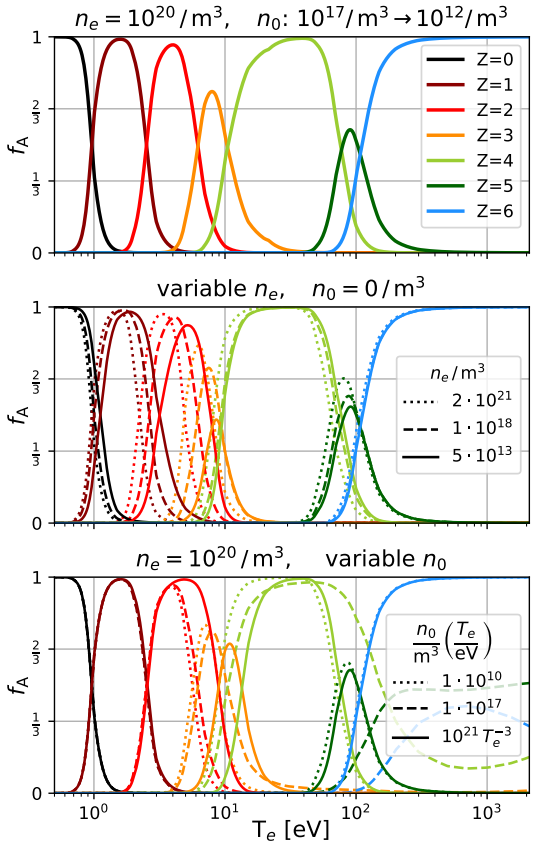

Figure 11: CRM fractional abundances of carbon ionization states in a hydrogen plasma depending on hydrogen n_0 and electron n_e density, plotted over electron temperature T_e. The top plot shows the result for typical densities in the plasma, with $n_0 \approx 10^{17}/\mathrm{m}^3$ below 10 eV, dropping to $10^{12}/\mathrm{m}^3$ at 1 keV.

In the above form, the CRM is a local model which is not able to describe any transport in the plasma without further modifications. Including transport can be done by building a list or a grid out of CRM and introducing interaction terms with neighboring cells. EMC3 assumes excitation state equilibration on timescales shorter than transport, but models the evolution of overall ionization stage densities like this. For each stage, EMC3 convects and diffuses the density in the cell to neighboring cells according to the simplified impurity model version of equations 9 to 11, implemented as sink/source terms for the densities. It also updates ionization stage densities in each cell using the ACD^z and SCD^z coefficients [21]. Radiation can then be calculated as in equation 14.

A less precise but simpler approach is to model the effect on transport on the ionization equilibrium in a global way with free parameters that can subsequently be optimized to fit more realistic models such as EMC3. The specific model optimized in the following subsection introduces τ_a and τ_s parameters acting as timescales for decay into more and less ionized states. For $n_{\mathrm{imp}}^{Z_{\mathrm{imp}}+1}$ and n_{imp}^{-1} defined as 0, it

can be written as

$$\frac{\mathrm{d}n^z_{\mathrm{imp}}}{\mathrm{d}t} = \frac{n^{z+1}_{\mathrm{imp}}}{\tau_a} + \frac{n^{z-1}_{\mathrm{imp}}}{\tau_s} - \frac{n^z_{\mathrm{imp}}}{\tau_a} - \frac{n^z_{\mathrm{imp}}}{\tau_s} \pm \text{SCD, ACD \& CCD terms}\,.$$

Often, a simple decay time τ with n^z_{imp}/τ as an additional loss is used as well.

The higher the density, the higher the rate of change into neighboring states. With a positive τ_a and only one populated ionized state, the state density would exponentially decay as e^{-t/τ_a}. Consequently, for a given temperature, increasing τ_a leads to an equilibrium with less density in highly ionized states, because total ionization is decreased. This is what is also expected from plasmas with transport from colder to hotter regions, as some less ionized impurities from their equilibrium at the lower temperature are always moved into the hotter plasma and did not have the time to reach the ionization equilibrium yet, decreasing the average ionization at that temperature. Equivalently, τ_s has the opposite effect, modeling transport from higher to lower temperatures.

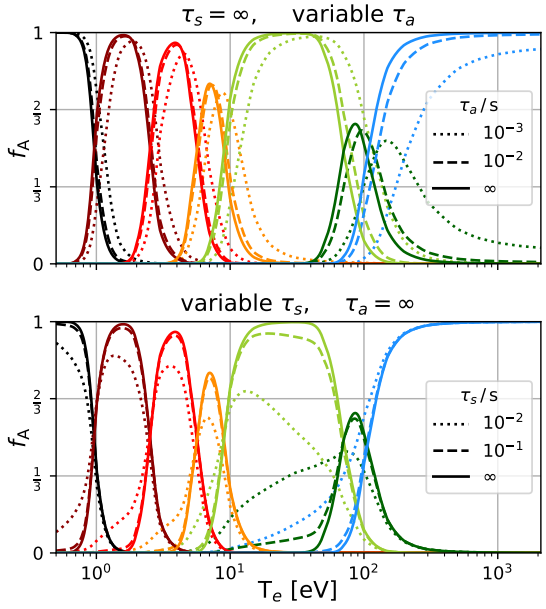

Figure 12: CRM fractional abundances of carbon ionization states in a hydrogen plasma as in figure 11, with $n_0 = 0/\mathrm{m}^3$, $n_e = 10^{20}/\mathrm{m}^3$ and varied τ parameters. $\tau = \infty$ indicates no transport.

3.4 Radiation Calculation from EMC3 data

For each simulated plasma, EMC3 provides the total radiation, electron and ion temperature, and the densities of all simulated species for every grid cell. In the cases without a given neutral impurity density n^0_{imp}, $n^0_{\mathrm{imp}} = 0$ is used. Given these quantities, emissivities E^z and radiation loss functions L^z can be calculated for each ionization stage z.

$$L'^z = \mathrm{PLT}^z(n_e, T_e) + \mathrm{PRB}^{z-1}(n_e, T_e) \tag{16}$$

$$E^z = n_e n_{\mathrm{imp}}^z L'^z \qquad L^z = f_A^z L'^z \tag{17}$$

$$E_{\mathrm{tot}} = P_{\mathrm{rad}} = \sum_{z=0}^{Z_{\mathrm{imp}}} E^z \qquad L_{\mathrm{tot}} = \frac{E_{\mathrm{tot}}}{n_e n_{\mathrm{imp}}^{\mathrm{tot}}} = \sum_{z=0}^{Z_{\mathrm{imp}}} f_A^z L'^z \tag{18}$$

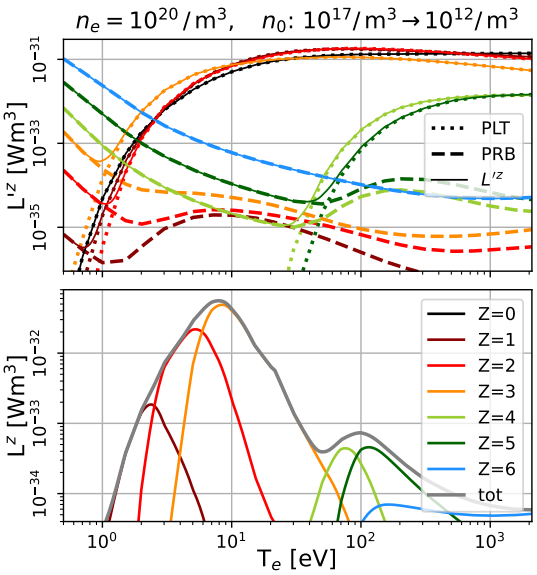

Figure 13: The top plot shows the PLT^z and PRB^z coefficients together with their sum, L'^z, for each carbon ionization state. At higher temperatures, line excitation radiation (PLT) dominates for each not fully ionized state ($z < 6$). L^z values with the densities from the first plot of figure 11 are shown in the bottom plot, together with L_{tot}. E^z has the same shape as L^z, as $E_z = n_e n_{\mathrm{imp}}^{\mathrm{tot}} L^z$.

Emissivities E^z give radiated power per volume, so by integrating the emissivity over the plasma, the total radiated power can be obtained. However, emissivities scale linearly with n_e and n_{imp}^z (see equation 13). Thus, L'^z is introduced as an electron- and impurity ion normalized quantity useful for comparison of radiation potential independent from the specific situation and reactor, still depending on electron density, but only for the shift in excitation state fractional abundances, not for the additional linear increase in radiation from increasing electron densities due to the increase in collisions. For a specific situation, the fractional abundances depending on temperature can be calculated and multiplied with L'^z to get the radiation loss functions L^z. They describe the radiation of each ionization stage per volume, electron and total impurity density and sum together to give the total radiation loss function L_{tot} at each T_e and n_e. L'^z is purely atomic data, while E^z and L^z are dependent on fractional abundances, and thus transport. Even though PRB increases for smaller temperatures at each ionization state, fractional abundances decrease for highly ionized states. Thus, PRB coefficients can be neglected for equilibrated plasmas, except at very high temperatures, where most impurities are fully ionized ($T_e \gtrsim 300\,\mathrm{eV}$ in figure 13).

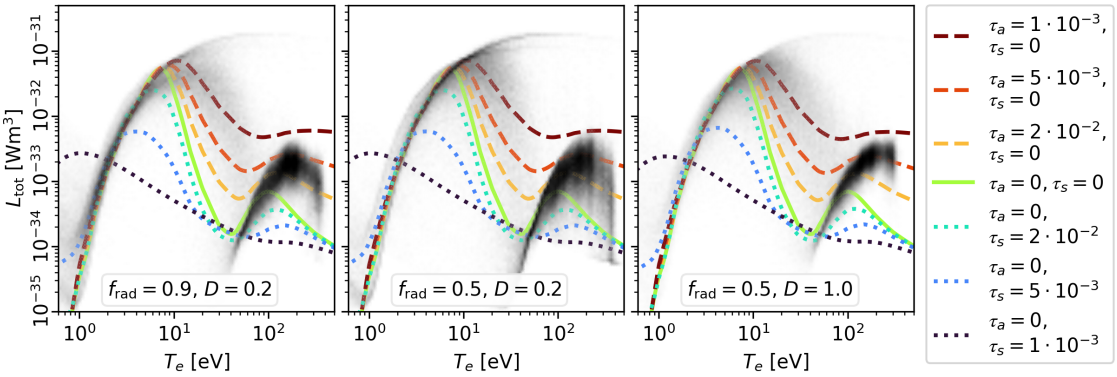

Figure 14: Total radiation loss function calculated via transport CRM model plotted against temperature, with varying τ-parameters. The densities in T_e, L_{tot} space for three representative EMC3 simulations for W7X plasmas are superimposed (adjusted for better visibility), varying in f_{rad} and D.

3.5 Transport τ-Model Comparison to EMC3 Simulations

Using representative EMC3 simulations for W7X plasmas described in more detail in the bolometry section (see figure 18), the CRM transport model can be investigated on how well it can model the radiation loss functions of the simulation plasma. L_{tot} is dependent on the fractional abundances, which in turn depend choice of τ-parameters, T_e, and to a much lesser extent n_e.

The simulation cells and CRM-data were binned along T_e only, and τ_a, τ_s were varied to fit the simulation data. Overall including a τ_s worsens the fit to the simulation data. Larger τ_a decrease the total deviation from the simulated values, but do not fit the shape better. Two bands of high cell number form for each simulation, shaped by the carbon impurity ions with $Z < 4$ and $Z \geqslant 4$. The low temperature band is fitted very well by the simple transport model, even with $\tau_a = \tau_s = \infty$, so transport is not relevant for $T_e < 10\,\text{eV}$. The high-temperature band on the other hand is not well fitted by any τ-parameter optimization, with $\tau_a, \tau_s < \infty$ together also only flattening the L_{tot} curve. n_e is almost constant for the high-temperature band, and even variations over the whole range of values also found in EMC3 cells only have a small

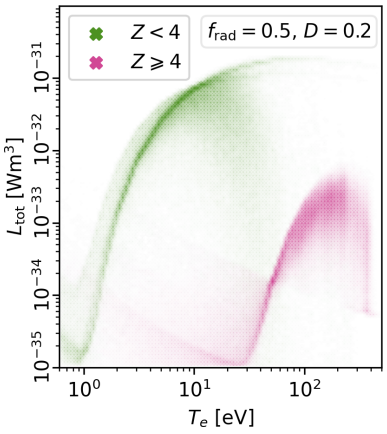

Figure 15: L_{tot} contributions for each cell in the simulation. Split by $Z < 4$ and $Z \geqslant 4$.

effect on the curve shape. The strong variability is not the effect of neutrals, as their effect on the impurity ionization distribution via charge exchange (CCD) is not modeled in EMC3. The stronger gradients in temperature further inside the plasma may be hypothesized to change the transport magnitude, so a variable τ_a increasing with higher temperatures would be needed. Between 8 eV to 60 eV, the bands connect. However, the connection is broad and the cell number is low, with the ends of the bands having much higher cell numbers. Here, cells with a large fraction of thrice ionized carbon impurities form the connection, with only once or twice ionized impurities extending the low-temperature band to above 10^2 eV. Thus, transport in W7X is strongly location dependent, with large differences of fractional abundances at similar temperatures at different positions in the plasma depending on the position in or outside the high emissivity bands. Optimizing radiated power when using the CRM calculated radiative loss function for each cell depending on temperature yields an optimum at $\tau_a \approx 5 \cdot 10^{-3}$ for simulations at representative W7X diffusion coefficients ($D \approx 0.2\,\mathrm{m^2/s}$). For larger normal and binormal diffusion coefficients $D \geqslant 0.5\,\mathrm{m^2/s}$, the optimum τ_a decreases ($\tau_a \approx 2 \cdot 10^{-3}$ at $D = 1\,\mathrm{m^2/s}$). Further work is needed to gain insight into the possibility of using local models to improve fit quality for the high and low-temperature bands.

Alternatively, future work can extend the τ-model to an extra parameter dimension: T_e. The τ-parameters can then simulate transport between temperature bins instead of imitating transport in one bin without any effect of distribution changes at other temperatures.

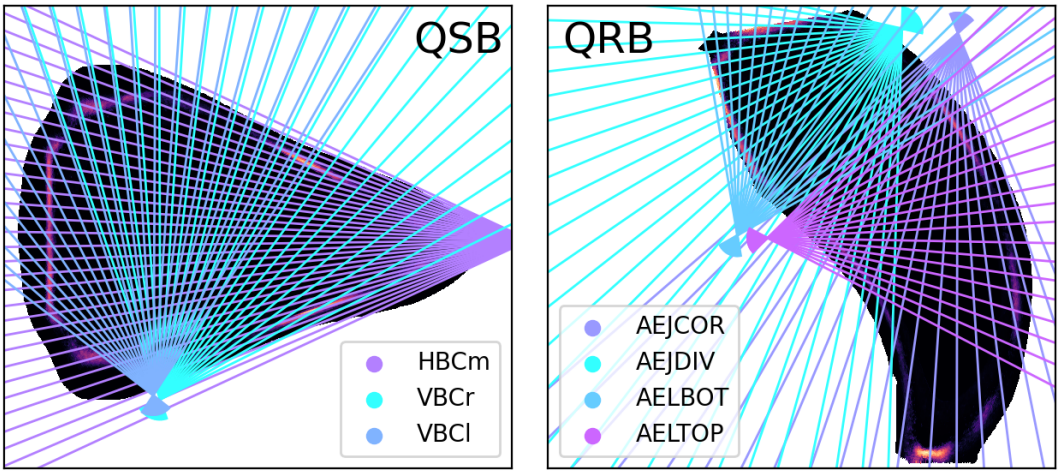

Figure 16: QSB and QRB cross-section bolometer sightlines. The QRB cross section is flipped vertically in W7X, but maps into the EMC3 grid like shown.

4 Bolometry

4.1 Concept and Use in W7X

Bolometers are measurement devices for radiation energy. A material is exposed to radiation and heats up from its absorption while being cooled by conduction to a heat sink. The absorbed energy can then be inferred from the value and rate of change in temperature. Normally, thin foils are used because they have a low heat capacity and consequently high sensitivity, causing large temperature changes from relatively little energy. This allows bolometer fans made from multiple foils with small cone volume of the lines of sight. Together, they can detect anisotropic radiative patterns. The foils are plated with meandering conductive traces, whose resistance increases together with the foil temperature, allowing radiation calculations from electrical resistance measurements. Such bolometers are used in W7X [37, 38]. Other concepts exist (like larger foils that resolve the radiation pattern via their temperature distribution, emitting infrared radiation able to be measured with infrared cameras), but will not be considered further in this thesis.

W7X possesses multiple bolometer fans in the up-down-symmetric triangle QSB cross-section or the QRB cross section 94° further in toroidal angle. Their central lines of sight are shown in figure 16. In operation, each foil provides a sightline integrated radiated power value, from which the full emissivity distribution can be reconstructed using tomographic methods. However, with less than 90 sightlines, even solving for a coarse 10×10 grid is a severely underconstrained problem.

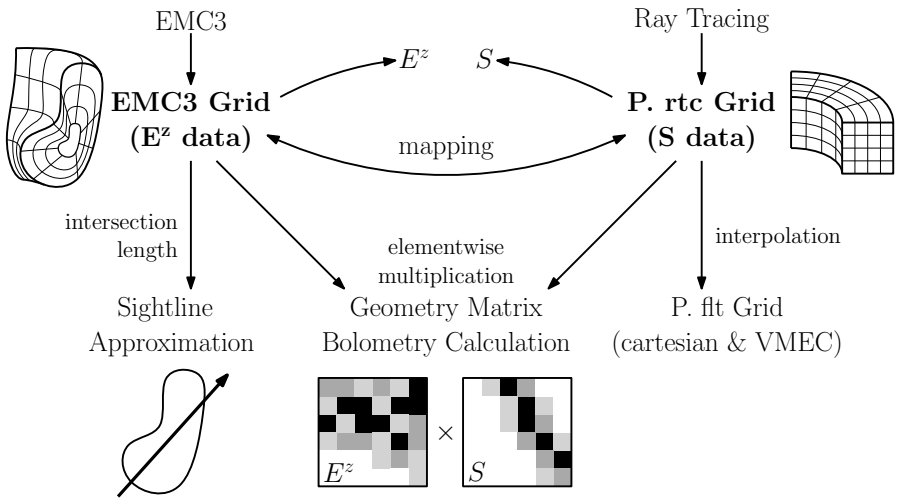

Figure 17: Bolometry data flowchart.

For the intended grids on the order of 140×512 ($r \times \theta$) cells, prior information about the expected emissivity distribution needs to be provided to constrain the possibility space and drive convergence to a realistic solution.

One aim of this section is to develop such restrictions on the shape of the emissivity distribution to be used in the tomographic reconstruction by investigating the properties of emissivity distributions in EMC3-simulated plasmas. Assuming a sufficiently good model, the restrictions will help in reconstructing faster and better emissivity distributions, and therefore better understanding of plasma behavior in W7X overall. The other aim is to perform synthetic bolometer measurements on the simulated data and investigate whether it allows inferring plasma properties directly.

4.2 Calculating absorbed Foil Power from Simulation Data

EMC3 simulates the plasma behavior and provides n_e and T_e to calculate emissivities E^z for each cell in the toroidal grid it is run on. However, the bolometer cones of vision get samples in a cylindrical grid (P. rtc Grid) by the Cherab python library [39]. Cherab is able to stochastically sample the cone of vision of a bolometer using Raysect, which was done by Gabriele Partesotti. In this thesis, QRB and QSB bolometers are investigated, with their sightlines around a toroidal angle of 202° (close to bean cross-section) and 108° (triangle cross-section). The stochastic sampling provides the bolometer sensitivity S for each cell, which is the volume it is taking up inside the bolometers code of vision, normalized via the foils etendue. This gives an effective volume that, multiplied by the radiation power per volume,

yields the total power $P = E^z \cdot S$ absorbed from the cell by the bolometer. For all cells c in the grid used for calculation, $S \propto V_c \, E_{\mathrm{tot,c}} / (\vec{r}_{\mathrm{Bol.}\to\mathrm{c}})^2$. Either E^z or S needs to be mapped from one to the other grid (EMC3 vs. P. rtc) to calculate the total power absorbed by an elementwise cumulative product. This was done in both directions to get a sense of the variations introduced by the interpolation mapping method used. Differences were insignificant (see subsection 4.4).

With a small cone of vision, the single line of sight $\Omega \to 0$ limit may be used to approximate and simplify the calculation of the absorbed power. Instead of a 3d integration over the cone, the emissivity needs to be integrated over the central ray only, and multiplied by the foil etendue. Given the location and direction of the bolometer sightline, the absorbed power can then also be calculated directly from the EMC3 grid. For all bolometer foils B with sightlines B_s, foil etendue $\mathrm{d}G_B$ and the length $L_{B_s,c}$ of the sightline B_s in the cell c,

$$P_{\mathrm{absorbed},B_s} = \mathrm{d}G_B \cdot \sum_{c \in \mathrm{EMC3\ cells}} E_c^z L_{B_s,c} \,.$$

The three approaches are shown conceptually in figure 17, with the mapping and line integration plots given in the appendix (section 6.2). The methods are compared in subsection 4.4 about synthetic measurements (figure 35).

4.3 Investigating simulated Plasmas

4.3.1 Restrictions on Cross Section Emissivity Distributions

Figure 18 shows all simulations investigated, and already demonstrates consistent radiation distributions with overall larger changes in emissivity perpendicular to the flux surfaces (radially, normal) than parallel to them in the cross-section (poloidally, binormal). This is reasonable because binormal transport dominates against normal transport, smoothing out distributions poloidally. Flux surfaces in the maximum emissivity regions form islands.

The emissivity structure, however, seems not to be influenced by the island structure. For the EIM magnetic configuration used in the investigated simulations, a flux surface enclosing all islands exists. Interpolating between the separatrix and the enclosing surface, and from the enclosing surface to the plasma vessel yields intermediate surfaces mimicking flux surfaces ignoring islands, subsequently called effective flux surfaces. The emissivity structure follows the effective flux surfaces.

Averaging emissivities on the effective flux surfaces and plotting radially yields figure 19. Inside the separatrix, temperatures are high (see figure 23), so carbon impurities are highly ionized and their radiation loss function is smaller (figure 13) then for the colder impurities further out. Inside the islands, temperature decreases

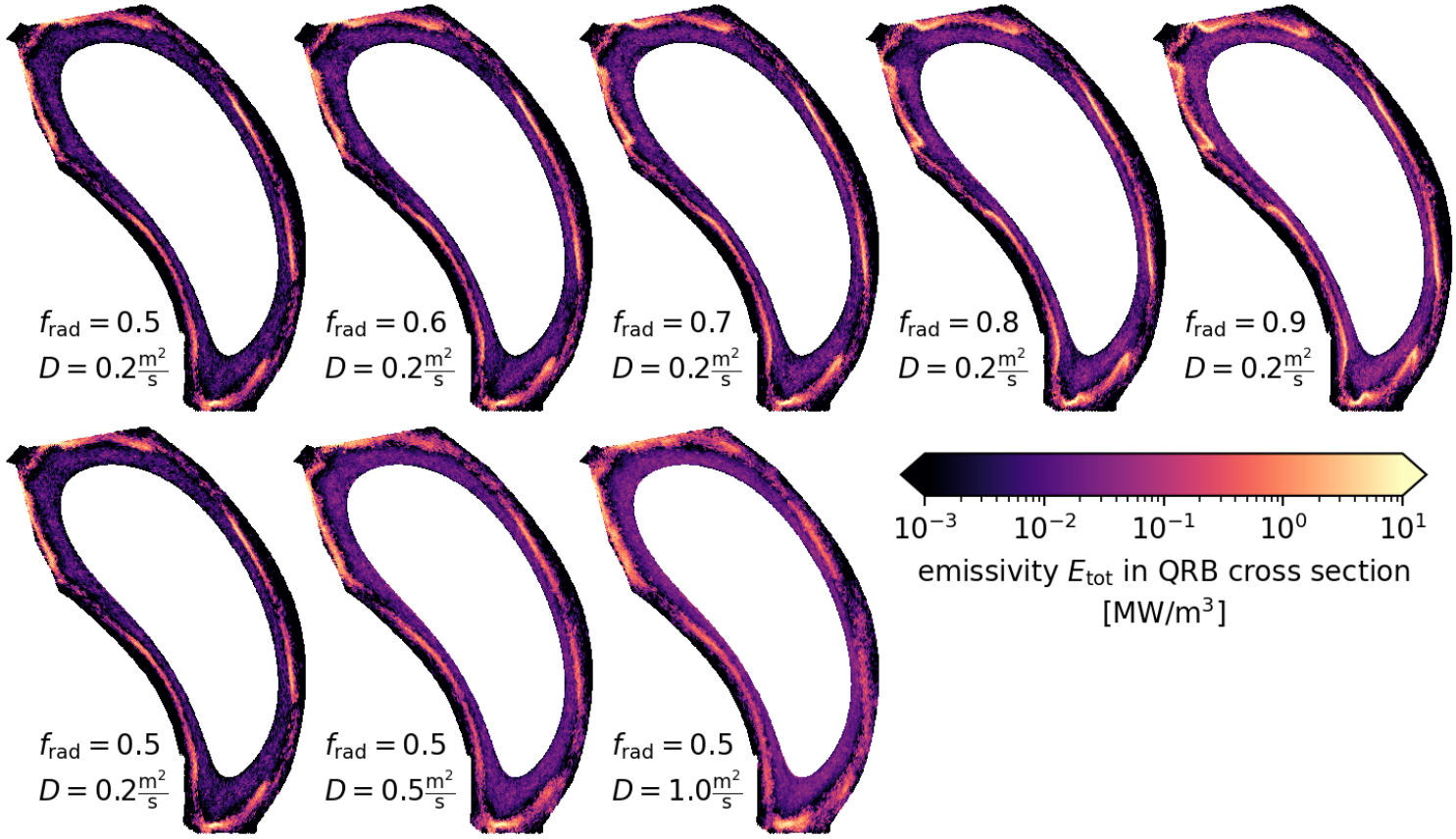

Figure 18: Simulated carbon impurity plasmas were investigated for the change in behavior for changing plasma parameters, with the emissivity E_{tot} shown in the QRB cross-section. All have 5 MW of heating, $f_{\text{rad}} \cdot 5\,\text{MW}$ of radiation and an electron and ion density of $3 \cdot 10^{19}/\text{m}^3$. The diffusion coefficient D and radiation fraction $f_{\text{rad}} = P_{\text{rad}}/P_{heat}$ differ between the simulation cases. The focus lies on the $D = 0.2\,\text{m}^2/\text{s}$ as they emulate the actual diffusion in W7X best with the current model [40].

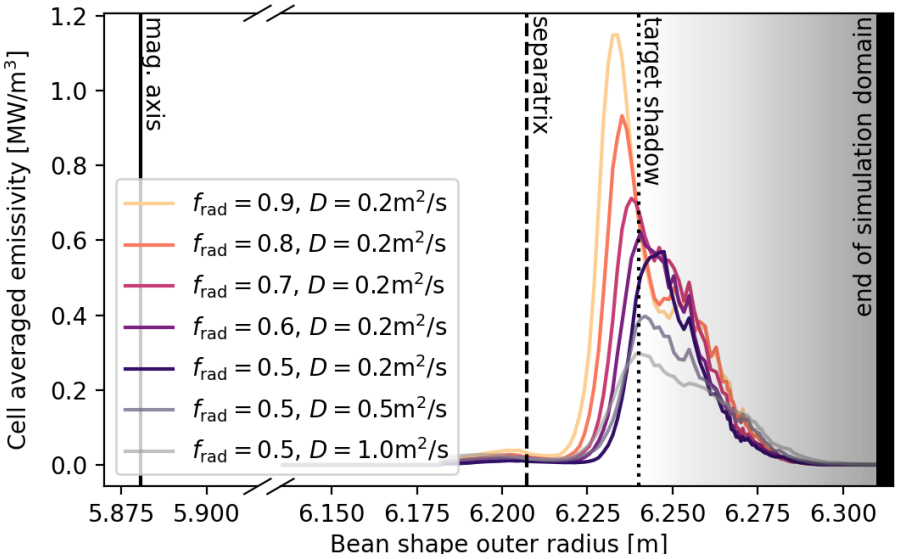

Figure 19: Total emissivities E_{tot} averaged over the flux surfaces and plotted outwards from the magnetic axis to the end of the simulation domain. Emissivities reach their maximum close to the targets.

and emissivities increase, getting smaller further out when the first targets get intersected by the flux surfaces and densities drop in the target shadows.

Higher diffusion coefficients in normal and binormal directions increase radial transport and smooth out the radial emissivity distribution as stated above, while larger radiation fractions increase the peak size due to the rise in radiation. However, larger radiation fractions also shift the target-undisturbed part of the peak inwards, shown in more detail in figure 20. This can be understood as more of the plasma energy being radiated away instead of being transported further outwards for higher f_{rad}. The FHWM may be capped by the distance to the target, as the target stops emissions at its surface, but the FWHM also decreases for high radiation fractions (not investigated). The emissivity drift inwards is also shown in figure 21, with the outer island flux surfaces (green) and the effective radius of maximum emission (blue) superimposed. For the sake of detail and clarity in visualization, some of the cross-section plots will focus on islands 4 and 5 as a stand-in for all of them. They are particularly interesting because they cross a target in the QRB cross-section.

Continuing with the poloidal pattern, gradients seem to be connected to the island and target positions. Figure 21 gives the impression that radial and poloidal behavior are roughly separable around the maximum emissivity effective cross-section with a periodic poloidal pattern, changing amplitude depending on the

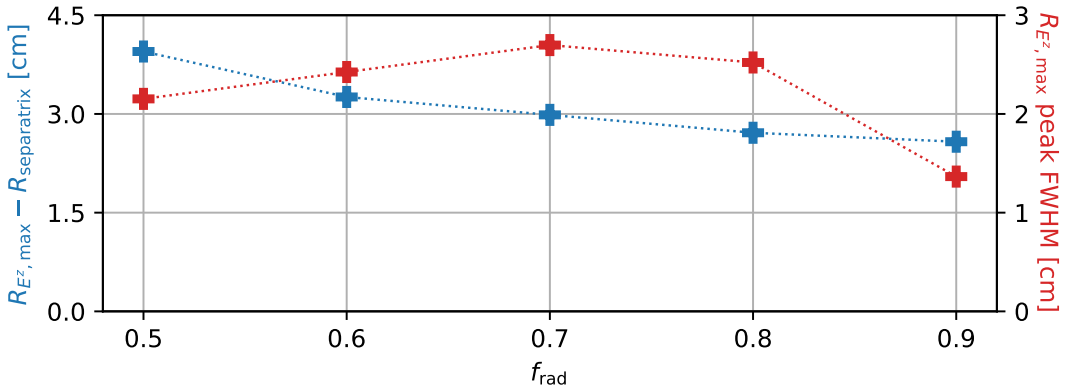

Figure 20: Radial emissivity maximum and its full width half maximum (FWHM) plotted against the simulation f_{rad}. In simulations with higher radiative fractions, the maximum moves inwards, closer to the separatrix.

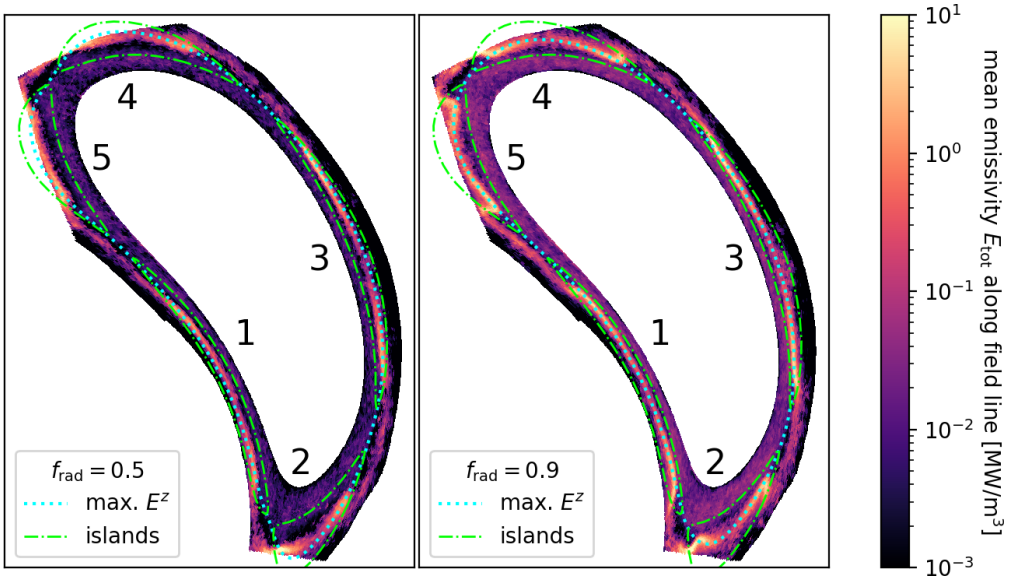

Figure 21: Field line averaged emissivities shown in the QRB cross section for the $f_{\mathrm{rad}} = 0.5$ (left) and $f_{\mathrm{rad}} = 0.9$ (right) simulation with $D = 0.2\,\mathrm{m}^2/\mathrm{s}$. Island contours and the contour of the maximum emissivity effective radius are overlaid.

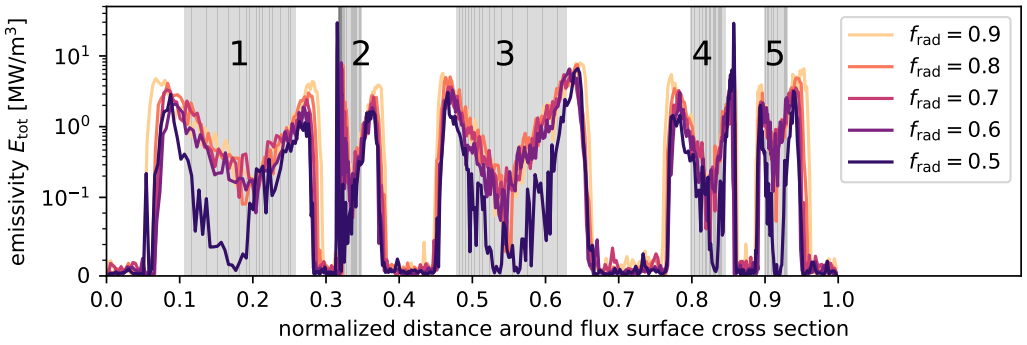

(a) Differences in poloidal emissivity depending on f_{rad}. ($D = 0.2\,\text{m}^2/\text{s}$)

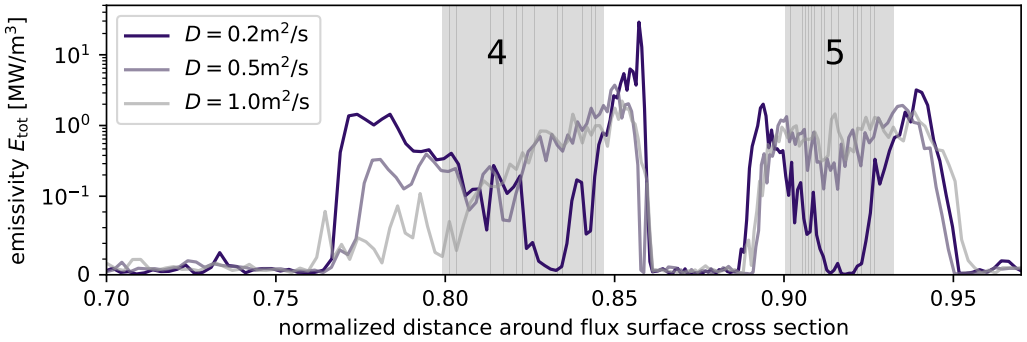

(b) Differences in poloidal emissivity depending on D. ($f_{\text{rad}} = 0.5$)

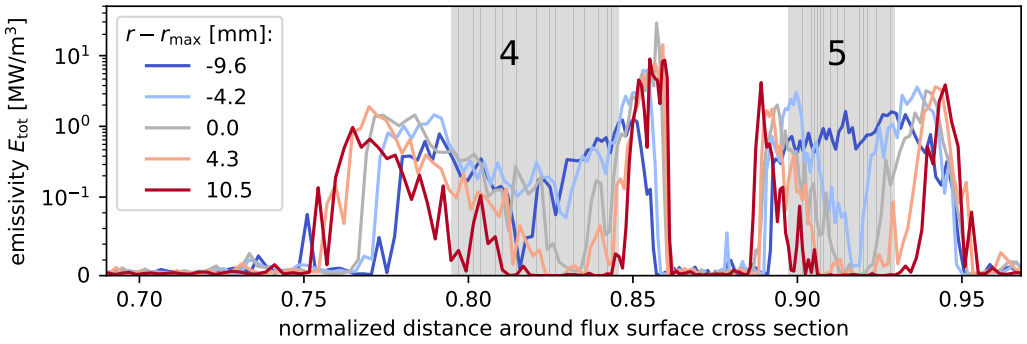

(c) Differences in poloidal emissivity depending on effective radius. ($f_{\text{rad}} = 0.5, D = 0.2\,\text{m}^2/\text{s}$)

Figure 22: Poloidal distribution of field line averaged emissivities at and around the effective radius of maximum emissivity. The poloidal position is parameterized as the normalized distance around the flux surface at the QRB cross-section, with an arbitrary constant starting point. Distances with maximum emissivity effective flux surface field lines partially in the target shadow for $f_{\text{rad}} = 0.9$ are shaded in grey.

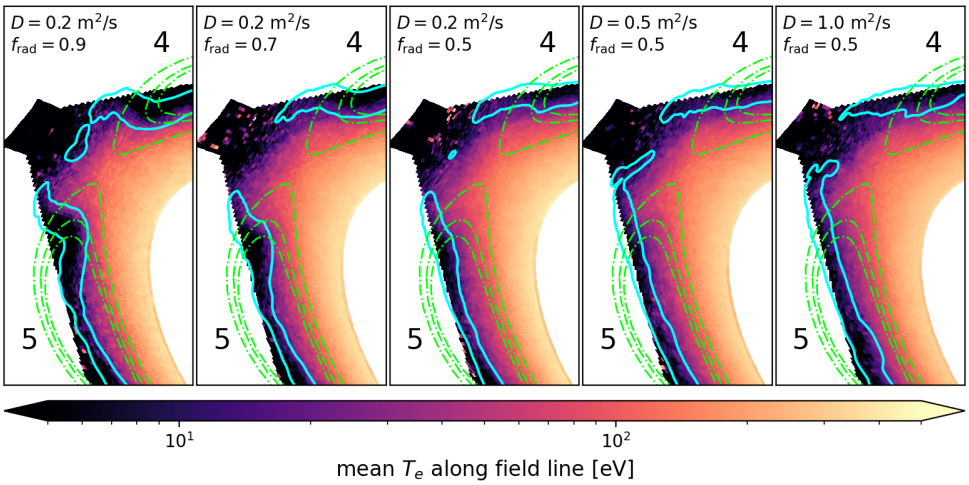

Figure 23: Electron temperatures in the QRB cross-section for multiple simulations. Regions of high radiation are shown as a cyan contour and follow closely along the 10 eV edge. Islands 4 and 5 are superimposed in green.

effective radius. The main poloidal emissivity pattern shown in figure 22a consists of a pattern repeating in and around every island. Close to the edge of the island, peaks in emissivity form and trail off exponentially toward the island center. In the direction out of the islands, emissivity drops almost immediately to the noise floor. Looking at figure 22c, it can be seen that the shape does change for different radii. Closer to the target, the drop-off in the center is more severe as more field lines are intersected. Further away from the target, the effect reverses. However, poloidal peak positions mostly do stay the same, with one exception being the outer edge of island 4, where the maximum moves toward island 3 when increasing the effective radius (see figure 21 right plot).

As an aside, the radiation region and radiation peak position are restricted by the temperature distribution via the ionization equilibria, and conversely, the temperature distribution is also constrained by the radiation, transferring heat energy away and preventing further heat transport outwards. This leads to the close relationship between temperature and radiation shown in figure 23.

The peak behavior is potentially also explained by the target interaction and inner island flux surface shapes. Radiation occurs before the particle interaction with the targets, with the field lines between the peaks hitting the target and passing through the space toroidally between targets (target shadow). The target shadow has lower electron and impurity densities, resulting in decreased emissivities. And while the maximum emissivity effective flux surface, is almost parallel to the is-

land flux surface at some point the inner island flux surfaces bend back. Figure 24 shows how the max. E_{tot} surfaces in grey are parallel to the green island surfaces in the middle of the islands and perpendicular near the ends. At this point transport along the effective field line switches from parallel to normal transport, leading to the immense emissivity drop-off. Higher normal and binormal diffusion counteracts target shadow effects and smooths gradients again as shown in figure 22b. For $D = 0.2\,\text{m}^2/\text{s}$, radiation on the field line in the middle of the island passing through the target shadow is below $10^{-1}\,\text{MW}/\text{m}^3$. At higher diffusion coefficients, the emissivity of this field line increases, and emissivity differences in the island decrease.

Looking at the movement of the emissivity peaks at the edge of the islands in figure 24, where the radiation zone changes alignment from effective flux surface to island flux surfaces reiterates the points made above. Emissions move further inward for higher radiation fractions, increasing the parallel surface part in the island (as long as it does not move too far) and moving the two island peaks further away from each other. For low radiation fractions, the maximum emissivity peak would move into the target, and is necessarily pushed outwards.

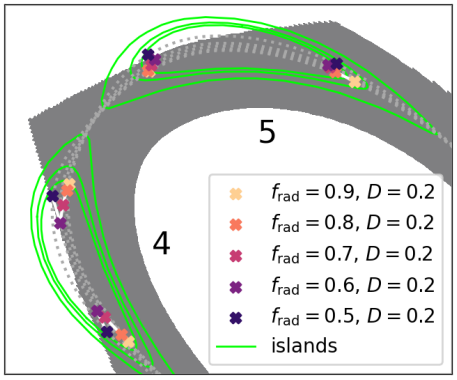

Figure 24: Movement of the emissivity peaks depending on f_{rad}.

For the reconstruction of a W7X plasma cross-section, and specifically the QRB cross-section, a procedure can now be defined. First, a radial distribution with one significant peak and variable position, width, and behavior in the target shadow can be fitted from the bolometer data. Then, high gradient poloidal sections are already roughly given, with the areas of maximum emissivity right next to them (see figure 24). This starting information, together with the constraints about the rough scale of normal and binormal gradients may finally be optimized by the tomographic methods to converge to a realistic emissivity distribution.

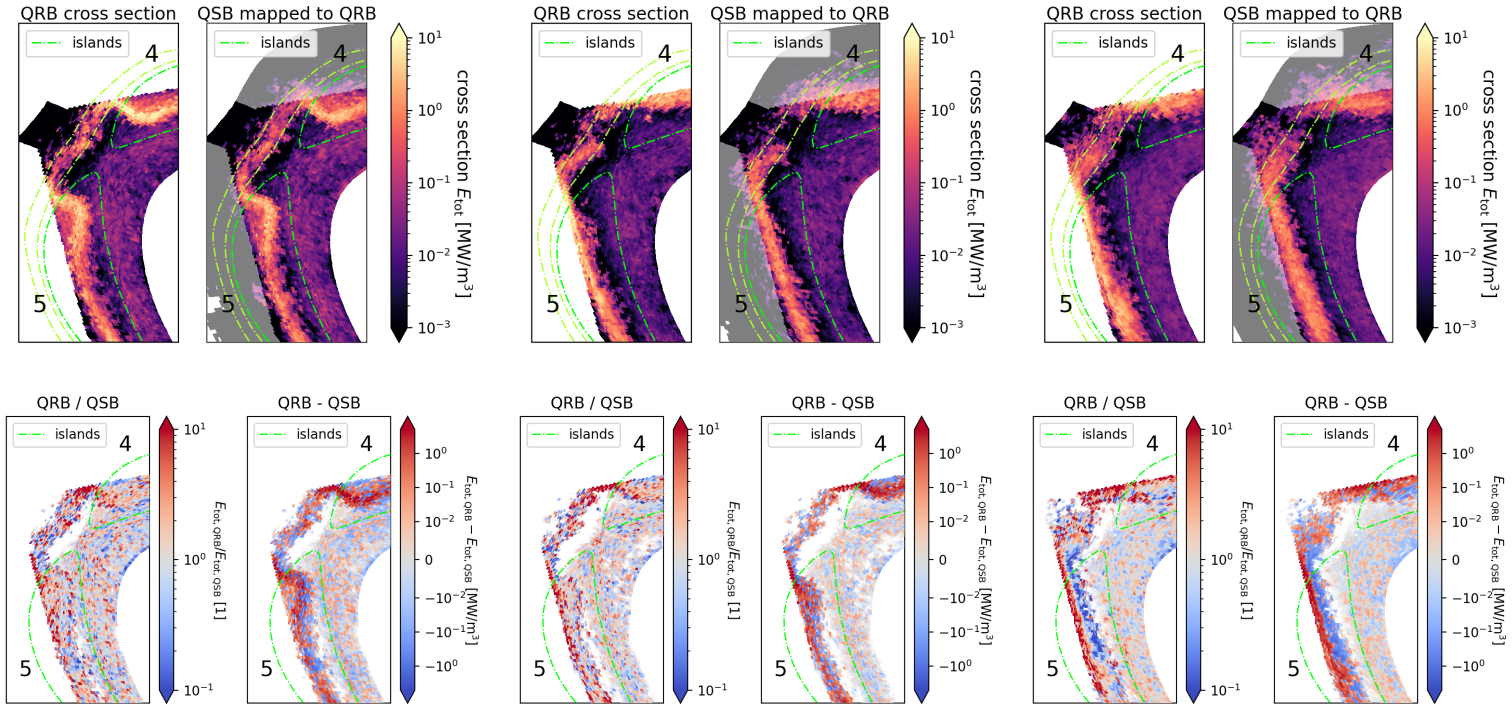

(a) $f_{\text{rad}} = 0.9$, $D = 0.2\,\text{m}^2/\text{s}$ (b) $f_{\text{rad}} = 0.5$, $D = 0.2\,\text{m}^2/\text{s}$ (c) $f_{\text{rad}} = 0.5$, $D = 1.0\,\text{m}^2/\text{s}$

Figure 25: Maps between the QSB and QRB cross sections along the field lines, shown in the QRB cross-section. The top plots visualize the emissivities in both cross sections. Because the QSB cross-section is not obstructed by targets, values exist for field lines that lie outside the plasma in the QRB cross-section. These still get mapped but are shaded in gray. The bottom plots quantitatively compare the QRB and QSB cross-sections, showing the fraction and differences between them. Red shaded cells signify larger emissivities in the QRB cross sections and blue larger emissivities in the QSB cross-section. Mean emissivities below 1 kW are not shown, as their contribution is insignificant (see figure 27). Some relevant (island) flux surfaces are overlaid in green.

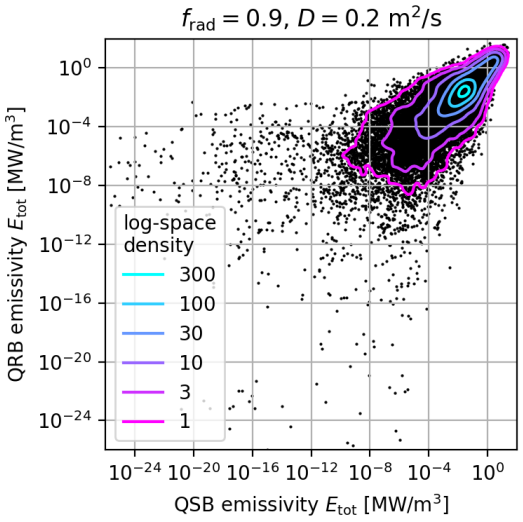

Figure 26: Logarithmic scatter plot of QSB and QRB emissivity of every effective field line. Density contours in the logarithmic space are superimposed.

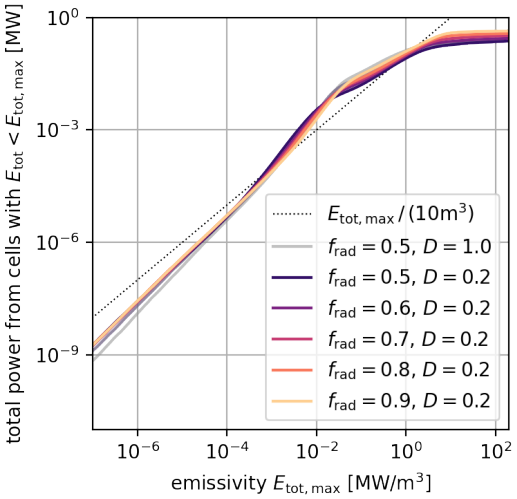

Figure 27: Integrated radiation power over cell emissivity. Cells with $E_{tot} \leqslant 1\,\text{kW/m}^3$ contribute less than 0.01% of the total power and can be ignored.

4.3.2 Mapping between Cross Sections

With the cross-section facing bolometers in the QSB and QRB cross-sections, a perfect mapping between them along field lines could potentially double the amount of data the topographic methods can use to reconstruct the emissivity distribution in any of those two cross-sections. However, the assumption of a perfect mapping can not be held up after the analysis done in figure 25. As can be seen from the top plots, emissivity does spread into the target shadows, flattening the emissivity peaks depending on their diffusion coefficient. At $D = 1.0\,\text{m}^2/\text{s}$, the effect is clearly visible, forming a band next to the QRB target, where the QRB radiation is much higher, with the adjacent areas on both sides showing higher QSB radiation. The target side is not shown in figure 25, but is trivial, as no radiation occurs outside of the target in QRB. For a lower normal and binormal diffusion coefficient, the decrease in radiation directly at the target still occurs. However, the simulation noise masks any other behaviors, except that total radiation seems to decrease when going from QRB to QSB, discussed further in subsection 4.3.3.

Disregarding the physical location of the effective field lines and solely focusing on their QSB and QRB emissivity values gives a relation depicted in figure 26, easier to quantify, and in which non-local effects may be seen more clearly. Scaling the

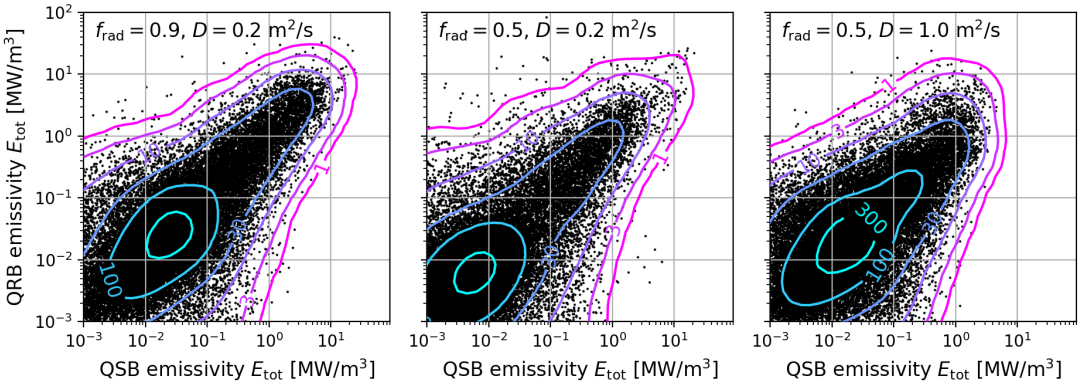

Figure 28: Logarithmic scatter plot of QSB and QRB emissivity of every effective field line for three simulations. Density contours in the logarithmic space are superimposed. Effective field lines undefined in any of the cross sections are ignored.

emissivities linearly puts too much focus on a few high-emissivity cells, with most cells pushed into the corner around 0, while in log scaling, the simulation noise for cells with $E_{tot} \approx 0$ has the opposite effect. But as low emissivity cells do not contribute much to the overall radiated power, they may be ignored.

For that reason, the amount that cells with E_{tot} smaller than a reference value $E_{tot,\,max}$ contribute was calculated and is shown in figure 27. Radiation power contributions increase roughly linearly with $E_{tot,\,max}$, before plateauing above $1\,MW/m^3$ because the number of cells at that level diminishes. Cells with $E_{tot} \leqslant 1\,kW/m^3$ contribute less than 0.01% of the total radiated power in each simulation and were thus chosen as a low emissivity cutoff. With this constraint, the QSB QRB relation is shown for the high and low radiation fraction, and high diffusion case in figure 28.

Higher radiative fractions pull the whole distribution upwards, while a higher diffusion coefficient pulls everything towards the middle, again with the effect of lessening emissivity differences. Somewhat surprisingly, it does not decrease the width of the scatter, although that can be explained by the QSB and QRB differences, ignoring the target intersecting field lines, being constrained mainly by the parallel, instead of the increasing normal and binormal diffusion when increasing D. From the slant in the distribution, greater variability in QSB is implied, consistent with the considerations above and the analysis of the total power ratio between the QSB and QRB cross sections in figure 29. Furthermore, in the investigated simulations, the power ratio decreases for higher radiative fractions, possibly because of fewer

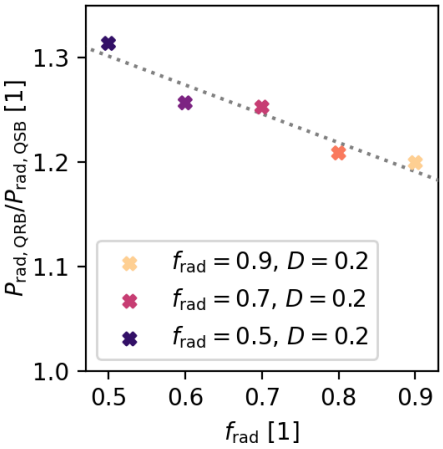

Figure 29: Total P_{rad} power ratio between QRB and QSB. QRB radiates more.

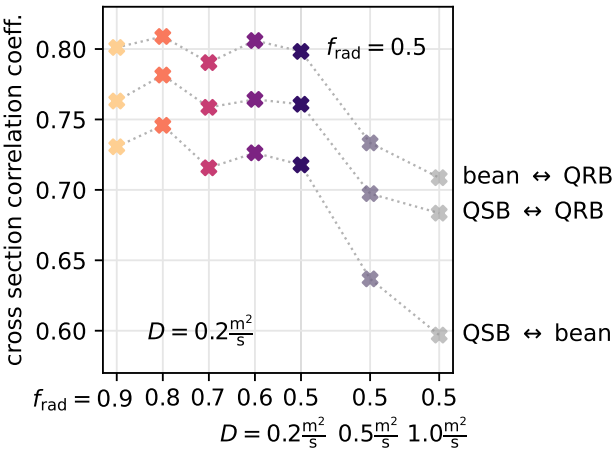

Figure 30: Correlation coefficient behaviour from figure 31 for selected cross-section comparisons.

target interactions in the QRB cross-sections. After enough calibration shots with external data about the radiation fraction, the sightline integrated radiation ratio between the QSB and QRB bolometer may be used as a fast phenomenological radiation diagnostic.

4.3.3 Toroidal Behaviour

Breaking away from specifically looking at QSB and QRB, a simple measure of likeness between to cross sections would be useful, and the log space scatter correlation ignoring emissivities less than $1\,\text{kW/m}^3$ in either cross-section, i.e for the points in figure 28, seems suitable for the same reasons the scatter plot was used in the first place. With either a few high emissivity or noise-dominated low emissivity cells dominating the correlation otherwise.

In the simulations, the toroidal resolution was chosen much coarser (1 cell/6°) than the poloidal and radial ones because the high parallel transport along field lines limits the gradients, and therefore toroidal changes in emissivity over small distances. For the 6 resulting cross sections, pairwise correlations were calculated and are shown in figure 31.

Only the difference in toroidal angle between two cross sections shows an effect on correlation, with the specific cross sections seemingly irrelevant. Concerning simulation parameters, changing radiation fractions do not significantly decrease correlation, while increasing normal and binormal diffusion does. Both effects

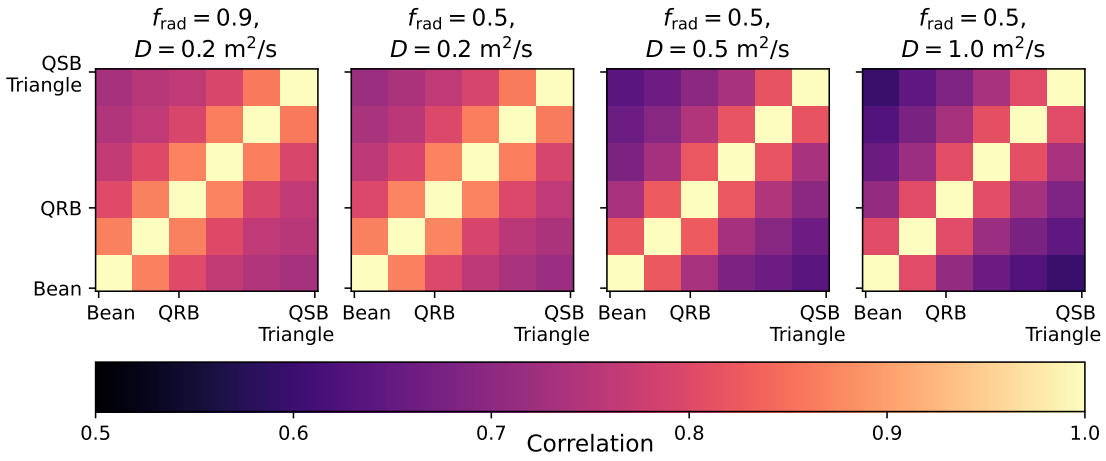

Figure 31: Correlation between any two cross sections for simulations with decreasing F_{rad} and increasing D. Calculated is the Pearson correlation coefficient between the $\log_{10}\left(E_{\text{tot}}(\text{cell})\right)$ data-sets of each cross-section.

are illustrated in figure 30 for the three relevant cross-section comparisons. This reiterates the conclusion that increased diffusion decreases cross-sectional similarity. The decrease in correlation is not linear nor consistent between cross-section comparisons, but this is also not expected with the somewhat ad hoc correlation restrictions.

Further analysis is needed to quantify the relationship between toroidal cross-section similarity and diffusion. However, assuming again the low diffusion coefficient of $D = 0.2\,\text{m}^2/\text{s}$ for W7X, close cross sections in normal circumstances may already reasonably be mapped onto each other to increase tomography accuracy independently of the radiation fraction.

Looking at the toroidal power distribution in figure 32, the much higher radiation between 0° and 18° is immediately noticeable. This is the toroidal region, where the targets get closest to the separatrix and induce radiation. Between the highest and lowest radiation cross sections, total radiated power differs by up to a factor of 2 which can not be ignored when mapping. Focussing on the QSB and QRB cross sections and their ratios gives figure 29 already discussed above. Finally, The variation in emissivity along effective field lines was investigated without averaging over the cross sections first. The relevant high emissivity field lines mainly follow the cross-section averaged emissivity from figure 32 as a whole, but with immense changes between single effective field lines. No information could be gained with

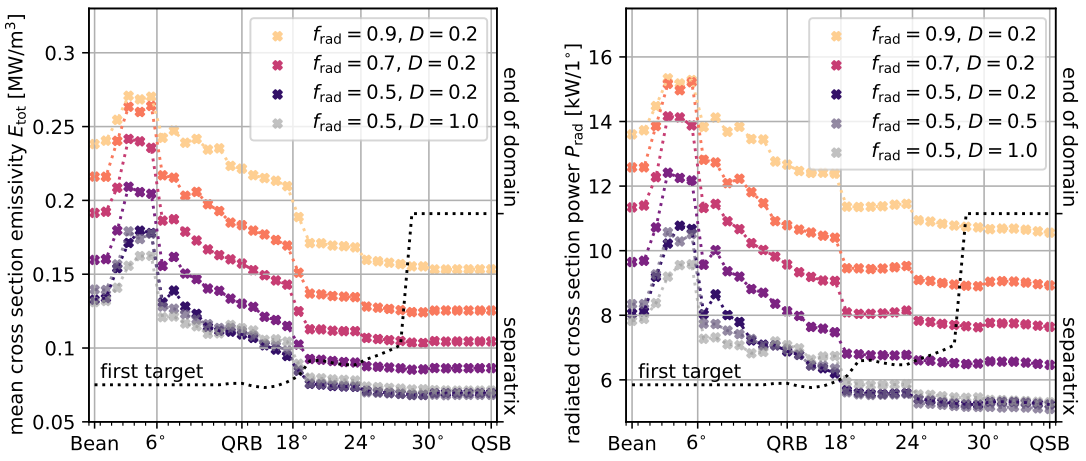

Figure 32: Mean cross-section emissivity (left) and total radiated power in the 1° wide cross-section (right), plotted against the toroidal angle.

that approach because the highest emissivity lines again dominate and inflate standard deviations between lines.

To make variations in emissivity comparable between for effective field lines with large ranges of emissivity, the coefficient of variation (σ/μ) was calculated for each effective field line, and then averaged together with the lines of similar mean emissivity to yield figure 33. For the few highest emissivity effective field lines, the statistics break down, while for low emissivity lines, simulation noise artificially increases the coefficient of variation. Quantization of the simulation noise was not possible, with neither normalization with the cross-section mean for each point, nor removal of the linear component of each line yielding differently shaped curves indicat-

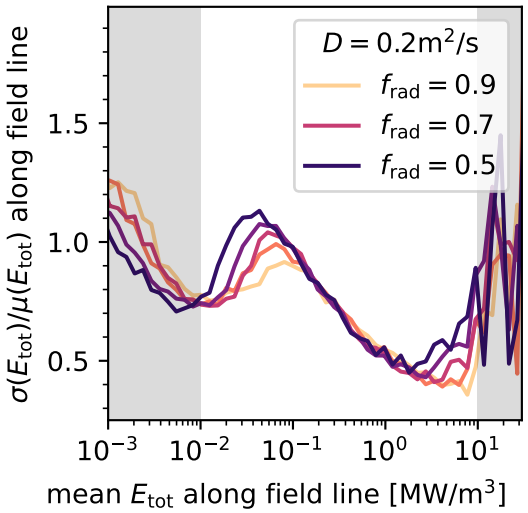

Figure 33: Coefficient of variation along effective field lines, binned and averaged along mean emissivities.

ing the noise limit. However, simulation noise should increase for smaller emissivities, so the local increase around $10^{-1}\,\mathrm{MW/m^3}$ can not be a noise artifact.

The region inside the separatrix is in the emissivity range of around $10^{-1}\,\mathrm{MW/m^3}$. Its radiation comes mostly from the C^{4+}, C^{5+} and C^{6+} carbon impurities with high radiation loss functions, and higher temperature, but lower electron and impurity density. However, it is stable toroidally due to effectively no target interactions and pulls down the coefficient of variation. Therefore the high coefficient comes from the island adjacent effective field lines and further analysis in the future is needed to understand why lines in the $1\,\mathrm{MW/m^3}$ range are less affected.

4.4 Synthetic Measurements

With knowledge about sightline and emissivity behavior for changing radiation fractions and diffusion coefficients, the sensitivity of the bolometers to the changing behavior can be investigated. The main aim of this subsection is to check if the inwards movement of the maximum radiation areas can be detected directly via the sightlines close to and parallel to the plasma edges.

First, the type of synthetic measurement needs to be chosen. Figure 35 compares the infinitesimal sightline integration with the mappings of emissivity from the EMC3 to the P. rtc grid and sensitivity from the P. rtc to the EMC3 grid. Both mapping approaches agree to within $10^{-9}\%$ for each examined simulation, so mapping inaccuracies are insignificant. The sightline approximation can decrease computational effort but disregards the cross-sectional area of the cone of vision. It deviates from the geometry matrix approach in the cases where it closely misses or hits an area of high radiation or gradients perpendicular to the line of sight are significant in the cone of vision. As the effective radial distribution of the high emission areas is small (see figure 19 and 38), a sightline only passing shallowly through the edge plasma will have the highest deviations. Only taking more central sightlines into account, errors decrease but stay at up to 50%. When using the sightline approximation for precise calculations, care needs to be taken when using it for sightlines out of areas of low gradient perpendicular to the sightlines.

Problematically, this is exactly the use case that is supposed to be investigated. Thus, the infinitesimal sightline data may not agree with physical measurements of the same plasma, and the geometry-matrix-emissivity mapping product data is used. However, the cross-sectional area of the foils may result in smoothing out changes between foils, so the infinitesimal sightline data is still calculated to test if the inwards movement be seen without these interfering effects and if redesigned bolometers with thinner cones of vision would be useful. As the outer (high index) QRB AEJDIV and QSB HBCm foils narrowly pass through the plasma and

intersect one island along the binormal direction, their sightline integrated power was calculated and is presented in figure 34.

For the AEJDIV foils 24 and 25 there are hints of the maximum emissivity region moving inwards, because the absorbed power for foil 24 increases for higher radiation fractions, while the foil 25 power decreases. However, especially for the HBCM foils, the movement seems to be too small to detect with the current foil resolution. For confident f_{rad} predictions, higher resolutions are needed for the sightlines crossing islands, especially for the infinitesimal sightline approach, where the maxima aren't even intersected by the two foil for some simulations (i.e. $f_{\mathrm{rad}} = 0.7$). Smaller cones of vision would decrease averaging effects from integration over the area of vision localizing the maximum emissivity effective radius further. On the other hand, higher diffusion coefficients can definitely be detected by the outermost foils although without any confidence in the exact value. Especially since at such low total absorbed powers, emc3 model and experiment quantities disagreements have larger effects.

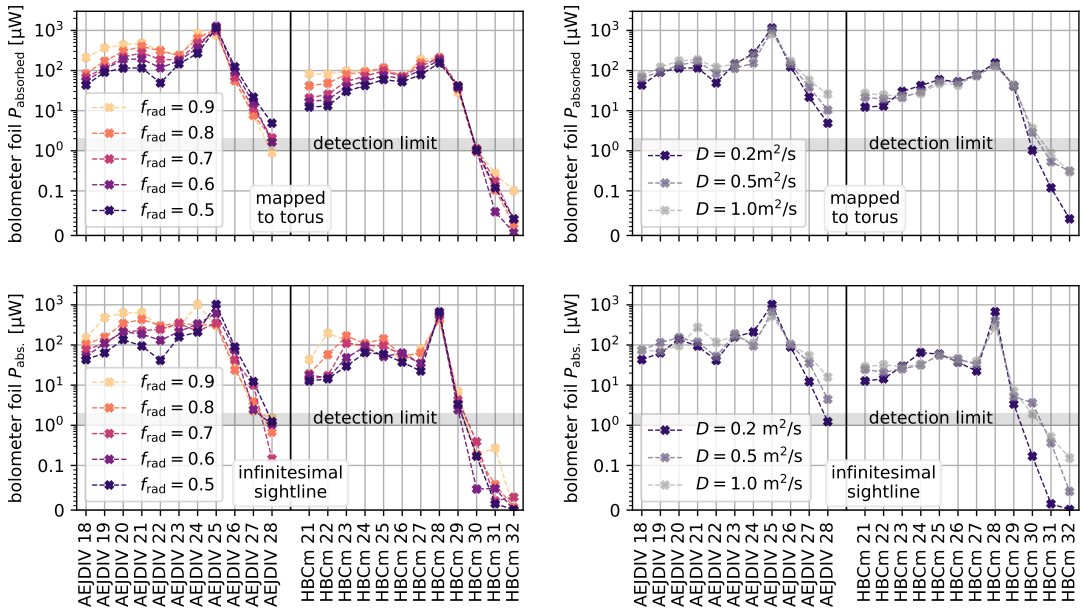

Figure 34: Synthetically measured absorbed power for the high index QSB HBCm and QRB AEJDIV foils. The data in the top plots was calculated by the geometry mapping approach, while the lower plots shows the absorbed power calculated by the infinitesimal sightline approach. The outer foil cones of vision do not cross the high emissivity regions anymore and drop off in value, bounded on the inside by the foil with maximum absorbed power crossing the emissivity peak.

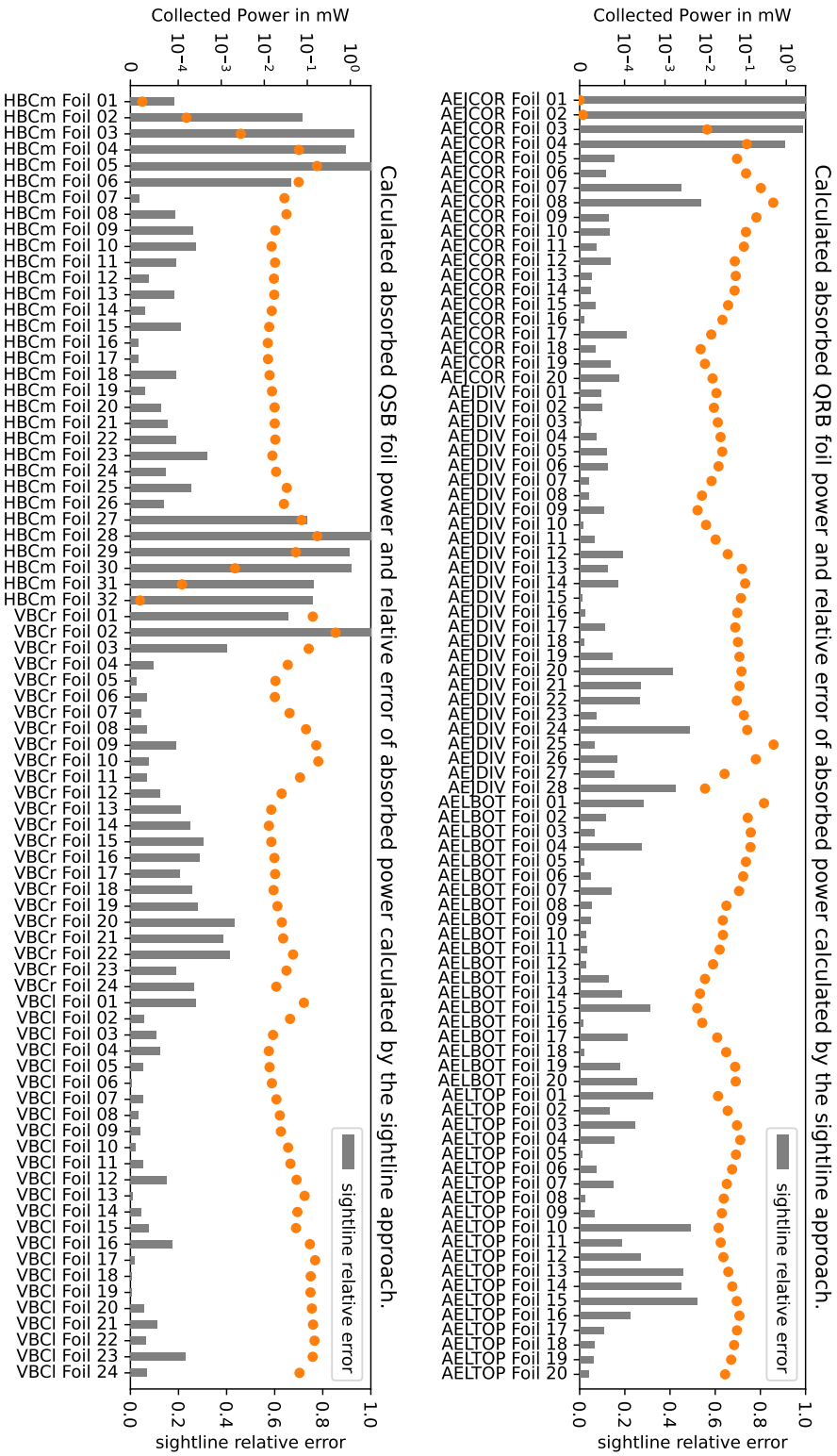

Figure 35: Comparison of approaches for calculation of absorbed power for bolometry foils. Both QRB (top) and QSB (bottom) for the N03.00_P05.00_D05_R02.00-C simulation are shown as an example. In most cases, the sightline approximation provides values with less than 50Large accuracy problems arise if the sightline just misses or intersects an area of high radiation.

5 Conclusion

To allow modeling non-rotationally symmetric W7X plasmas with EMC3/Eirene, a python EMC3-grid generation tool was adapted to handle full module and full torus grids. For plasmas with stochastic outer regions (FTM configuration), the tool was also extended to fit concave hulls around magnetic field line sets in the absence of closed flux surfaces. Methods to optimize EMC3-grids for numerical accuracy were developed and implemented as well. Optimized grids were generated for both use cases. A workflow for such grid generations and optimizations exists now and will be used in future work to investigate behavior in asymmetric W7X plasmas.

The applicability of ad hoc sink/source terms in the ionization balance of local CRM-based models to emulate radiation changes due to transport processes were investigated. Better agreements with EMC3 simulated plasmas in emissivity distribution and total emitted power was achieved than with a local model not including transport. Areas indiscernible with the τ-model but with strongly different behavior exist. Only separation of these areas in future work will make the τ-model able to approximate real plasmas to a useful degree.

Restrictions on possible emissivity distributions in W7X cross-sections were developed. The investigated plasmas show distributions localized around one r_{eff}, dependent on plasma parameters. The maximum emissivity band seems to follow an "effective flux surface". The surface moves inward when intersecting a target and outwards between island flux surfaces, giving a plasma parameter-dependent shape at the maximum emissivity region. Poloidal distribution of the high emissivity band are constrained by island flux surfaces, targets, and plasma parameters. The observed restrictions allow a strongly simplified approach to emissivity tomography, solving for the radial distribution first and optimizing the distribution to follow along a maximum emissivity "suggestion shape" afterward. Application of the approach to the tomography of experimental data is currently evaluated in other works of the W7X-team.

Finally, synthetic bolometry measurements on EMC3 plasmas were implemented to investigate if changes in plasma emissivities are able to be measured directly. Higher radiative fractions decrease the maximum emissivity r_{eff}, moving emissivity peaks inwards and decreasing absorbed power for bolometer foils with lines of sight tangential to the plasma edge while increasing absorbed power for neighboring foils on the inside. Changes are barely detectable in specific cases of low diffusion. With a higher bolometer resolution at the edges of the plasma, bolometers will be able to directly localize the radiation front.

6 Appendix

6.1 EMC3 Grid Comparison

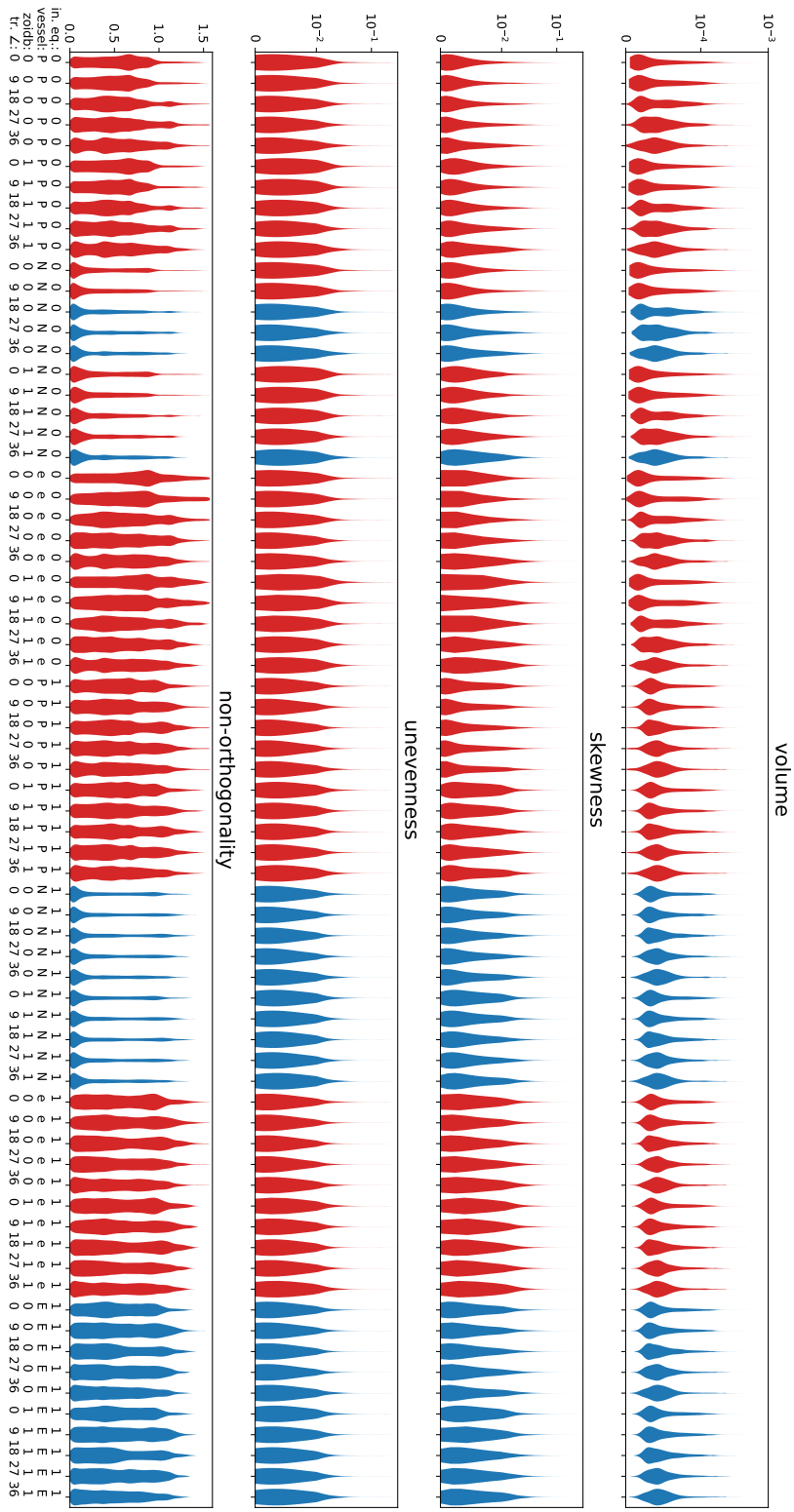

Figure 36: Grid quality measure plot to investigate the effects of the implemented grid optimization routines for all testing grids generated. Shown in the rows are the distributions of the volume and grid measures as defined in [26] over all of the cells of the grid. Each column is associated with one grid, generated by the parameters specified in the labels. Grids with concave or overlapping cells are indicated by a red color.

6.2 Bolometry Data Conversion and Integration

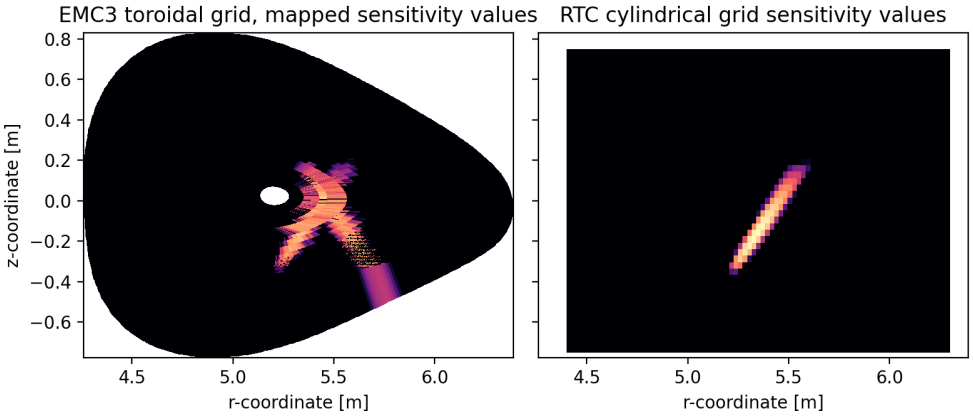

Figure 37: Sensitivity value S cell mapping from the cylindrical to the toroidal grid. The N03.00_P05.00_D05_R02.00-C simulation QSB data for VBCr foil 9 at $\phi = 1.87$ with an arbitrary colormap scale is shown as an example. Notice that the cylindrical grid is defined for the full cone of vision, while the toroidal grid ends at the triangular cross-section. Because of this, a part of the cone has been remapped into the toroidal grid and flipped for symmetry reasons.

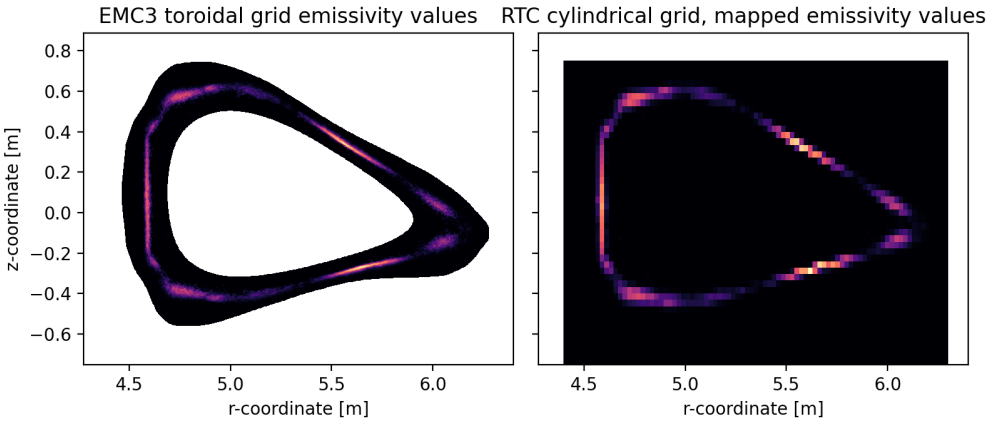

Figure 38: Emissivity value E^z cell mapping from the toroidal to the cylindrical grid. The N03.00_P05.00_D05_R02.00-C simulation $E^3(C^{3+})$ data at $\phi = 1.87$ with an arbitrary colormap scale is shown as an example. The white boundary in the cylindrical grid is an effect of the NaNs in the toroidal grid. But because no cell in the toroidal grid maps to the outermost parts of the cylindrical grid, far-out cells have the value 0 again.

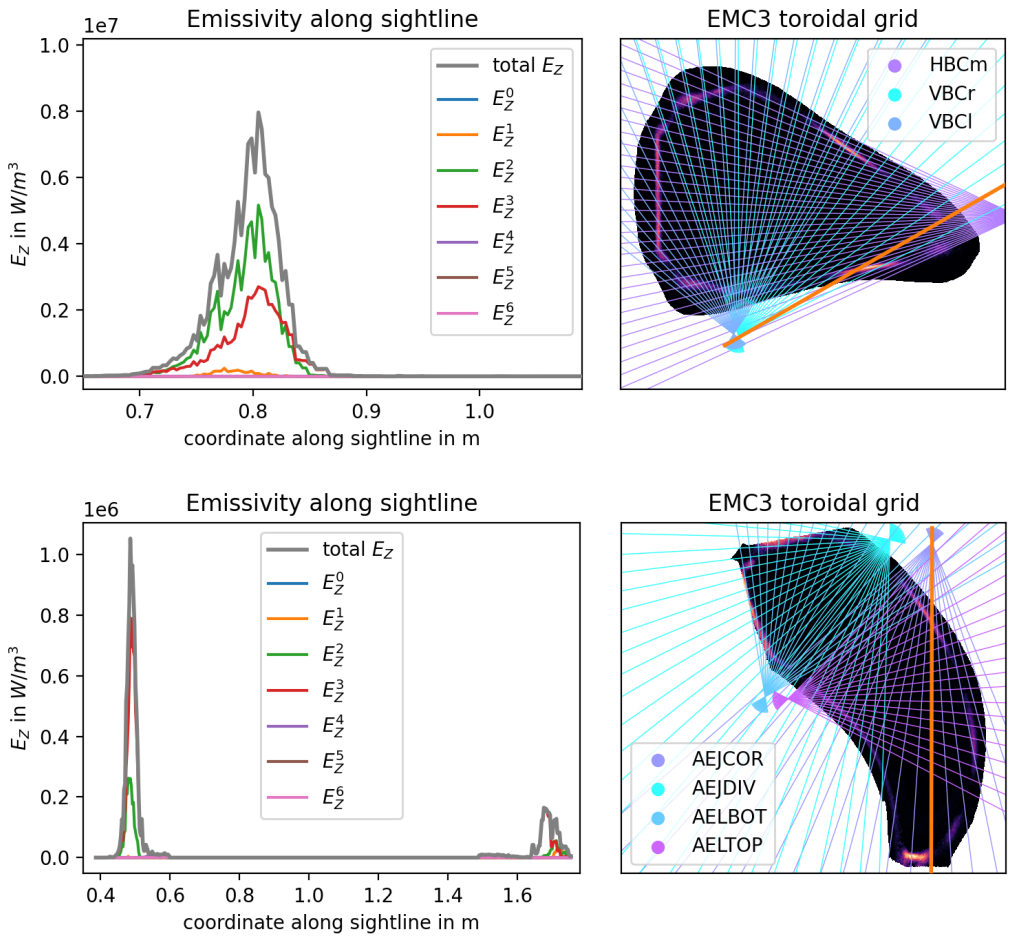

Figure 39: 1D line integration along a bolometer foil sightline. The QSB VBCr foil 2 is used for the top plot, and the QRB AEJCOR foil 7 for the bottom one. Both use the N03.00_P05.00_D05_R02.00-C simulation with an arbitrary colormap scale for the total emissivity.

6.3 Grid Measure Implementation

For a generated EMC3 grid g in the form of a $\#\tilde{r} \times \#\tilde{\theta} \times \#\tilde{\phi} \times 3$ array with (R, z, ϕ) cylindrical coordinates for each grid vertex, the following code calculates the grid measures from section 2.2 for every cell. The coordinates of a vertex with grid indices $(\tilde{r}, \tilde{\theta}, \tilde{\phi})$ are given by $g_{\tilde{r},\tilde{\theta},\tilde{\phi}}$.

```
# g[minor radius index][poloidal index][toroidal index]
#   = [major radius, vertical height, toroidal angle] (in meter)
#   = cylindrical coordinate of given indices

# not whole loop, only tenth of torus -> phi doesn't loop
def yield_grid_cells(g, r_lahead=1, tht_lahead=1, phi_lahead=0):
    g = g[:,:-1] # remove double tht=0,2pi values
    # implement general looping edges g[r,tht,phi,c]; tht loops, r, phi not
    ors, othts, ophis, _ = g.shape  # original g size
    g = np.pad(g, [(0,0), (0,tht_lahead), (0,0), (0,0)], mode='wrap')

    # create smaller output array
    h = np.zeros((ors-r_lahead, othts, ophis-phi_lahead,
                  1+r_lahead, tht_lahead+1, phi_lahead+1, 3))

    # iterate over all parameter coordinates
    for cr in range(ors-r_lahead):
        for ctht in range(othts): #tht loops
            for cphi in range(ophis-phi_lahead):
                h[cr, ctht, cphi] = g[cr:cr+r_lahead+1,
                        ctht:ctht+tht_lahead+1, cphi:cphi+phi_lahead+1]
    return h

# convert the direction dependent functions to one that
# returns the results of both directions as a tuple
def r_tht_direction_tuple(f):
    return lambda g: (f(g, 'r'), f(g, 'tht'))

def _cell_centers(g, x, direction):
    mid = np.mean(x[0:2,0:2], axis=(0,1))[0]
    if direction == "r":
        mid_af = np.mean(x[1:3,0:2], axis=(0,1))[0]
    else:
        mid_af = np.mean(x[0:2,1:3], axis=(0,1))[0]
    return mid, mid_af

def _facemid(g, x, direction):
    if direction == "r":
        facemid_af = np.mean(x[1,0:2], axis=0)[0]
    else:
        facemid_af = np.mean(x[0:2,1], axis=0)[0]
    return facemid_af
```

```
@r_tht_direction_tuple
def non_orthogonality(g, direction):
    assert direction == "r" or direction == "tht"
    ws = (2,1,0) if direction=="r" else (1,2,0)  # window size
    wv = yield_grid_cells(g, *ws)  # window view
    # the two directions of cell edges, along r and along tht
    rs, thts, phis = wv.shape[:3]
    # angles on faces
    af = np.empty((rs, thts, phis))

    # using numpy vector functions is fast, but takes ages to code. will loop
    for r in range(rs):
        for tht in range(thts):
            for phi in range(phis):
                x = wv[r,tht,phi]
                # cell centers
                mid, mid_af = _cell_centers(g, x, direction)
                # direction of cell midpoint connections
                v_af = (mid_af - mid)/np.linalg.norm(mid_af - mid)
                # direction of edges
                t_af = x[1,1]-x[1,0] if direction == "r" else x[1,1]-x[0,1]
                tn_af = t_af/np.linalg.norm(t_af)  # don't need normal
                # angle between edge direction and midpoint direction
                # angle(v,n) = arcsin abs (v.t)/(||v||*||t||)
                # with t tangential and n corresponding normal vector
                af[r,tht,phi] = np.arcsin(np.abs(np.dot(tn_af, v_af)))
    return af

@r_tht_direction_tuple
def unevenness(g, direction):
    assert direction == "r" or direction == "tht"
    ws = (2,1,0) if direction=="r" else (1,2,0)  # window size
    wv = yield_grid_cells(g, *ws)  # window view
    # the two directions of cell edges, along r and along tht
    rs, thts, phis = wv.shape[:3]
    # unevenness on faces, also named a
    af = np.empty((rs, thts, phis))

    # using numpy vector functions is fast, but takes ages to code. will loop
    for r in range(rs):
        for tht in range(thts):
            for phi in range(phis):
                x = wv[r,tht,phi,...,:2]
                # cell centers
                mid, mid_af = _cell_centers(g, x, direction)
                # direction of cell midpoint connections
                v_af = (mid_af - mid)/np.linalg.norm(mid_af - mid)
                # cell midpoint line midpoint m_f
```

```
                linemid_af = np.mean([mid, mid_af], axis=0)
                # cell corner connection line (edge) midpoint c_f
                facemid_af = _facemid(g, x, direction)
                # line distance to point
                ld_af = np.linalg.norm(np.cross(v_af, facemid_af-mid_af))
                # rotated cell mitpoint dir by 90 deg
                n_af = np.array([-v_af[1], v_af[0]])
                # check if needed to add or remove
                f_af = np.sign(np.dot(n_af, facemid_af-mid_af))
                # move corner connection line (edge) midpoint on line c_f'
                proj_facemid_af = facemid_af - f_af*ld_af*n_af
                # distance of c_f' and m_f
                num_dist_af = np.linalg.norm(proj_facemid_af-linemid_af)
                # distance between two cell midpoints
                den_dist_af= np.linalg.norm(mid_af - mid)
                # measure of unevenness
                af[r,tht,phi] = num_dist_af/den_dist_af
    return af

@r_tht_direction_tuple
def skewness(g, direction):
    assert direction == "r" or direction == "tht"
    ws = (2,1,0) if direction=="r" else (1,2,0)  # window size
    wv = yield_grid_cells(g, *ws)  # window view
    # the two directions of cell edges, along r and along tht
    rs, thts, phis = wv.shape[:3]
    # unevenness on faces, also named a
    af = np.empty((rs, thts, phis))

    # using numpy vector functions is fast, but takes ages to code. will loop
    for r in range(rs):
        for tht in range(thts):
            for phi in range(phis):
                x = wv[r,tht,phi,...,:2]
                # cell centers
                mid, mid_af = _cell_centers(g, x, direction)
                # direction of cell midpoint connections
                v_af = (mid_af - mid)/np.linalg.norm(mid_af - mid)
                # cell corner connection line (edge) midpoint c_f
                facemid_af = _facemid(g, x, direction)
                # line distance to point == ||c_f' - c_f||
                ld_af = np.abs(np.cross(v_af, facemid_af-mid_af))
                # distance between two cell midpoints
                den_dist_af = np.linalg.norm(mid_af - mid)
                # measure of skewness
                af[r,tht,phi] = ld_af/den_dist_af
    return af

def fast_convex(g):
```

```
    wv = yield_grid_cells(g, 1, 1, 0)  # window view
    wv =  wv[...,0,:2] # ignore phi component in cell and coord
    # the two directions of cell edges, along r and along tht
    rs, thts, phis = wv.shape[:3]
    # the check works in the way, that the cell has 4 edges and for
    # each edge (going counterclockwise), the other cell corners
    # need to be on the left side of the edge for the cell to be convex
    # cell edge directions along parameterisation in r and tht
    dir_r, dir_tht  = np.diff(wv, axis=3), np.diff(wv, axis=4)
    # we need to invert half the edge- (2nd in r and 1st in tht)
    # direction vectors so they point counterclockwise
    # views into dir_r, d_tht for easy access
    dir_r0, dir_r1 = dir_r[...,0,0,:], dir_r[...,0,1,:]
    dir_tht0, dir_tht1 = dir_tht[...,0,0,:], dir_tht[...,1,0,:]
    dir_r1 *= -1; dir_tht0 *= -1
    # now we need to check if the vectors in order of
    # r[0], tht[1], (-)r[1], (-)tht[0] are always turning left
    # from the last vector (between 0° and 180°).
    # cell convex IFF above true for all four edges
    cross_values = np.empty((rs, thts, phis, 4))
    cross_values[...,0] = np.cross(dir_r0, dir_tht1)
    cross_values[...,1] = np.cross(dir_tht1, dir_r1)
    cross_values[...,2] = np.cross(dir_r1, dir_tht0)
    cross_values[...,3] = np.cross(dir_tht0, dir_r0)
    # we can take the min > 0 to see if all of them are > 0
    is_convex = cross_values.min(axis=-1) > 0
    return is_convex

# calculate the cell volume of each cell.
# the surfaces with normals in r or tht directions are in general curved
# so we approximate the curved quad by two planar triangles.
# the line inside of the cell surface
# between the triangles either goes   (0,1) @-------------@ (1,1)
# from vertex[0,0] to vertex[1,1] or       / \.        ./'/
# from vertex[1,0] to vertex[0,1]. This   /    \. ./'   /    \. = 01->10
# coice is specified in triangle_cut     /    ./'\.    /    ./' = 00->11
# (dict) with either "00->11" or        / ./'      \. /
# "01->10" as the value correspond.    @-------------@ (r=1, tht=0)
# to the "r" & "tht" key.           (0,0)
def triangulated_volume(g, triangle_cut={"r":"00->11", "tht":"00->11"}):
    # we can fill the whole cell volume via 6 tetrahedrons
    xyz_g = np.empty_like(g)
    xyz_g[...,0] = g[...,0] * np.cos(g[...,2])  # x = r cos phi
    xyz_g[...,1] = g[...,0] * np.sin(g[...,2])  # y = r sin phi
    xyz_g[...,2] = g[...,1]                     # z = z
    wv = yield_grid_cells(xyz_g, 1, 1, 1)
    rs, thts, phis = wv.shape[:3]
    vols = np.empty((rs, thts, phis))
    subvols = np.empty(6)
```

```
    if triangle_cut["r"]=="00->11" and triangle_cut["tht"]=="00->11":
        prism_tetra = _tri_antiprism_tetrahedrons([
            (0,0,0), (0,1,1), (1,1,0), (0,0,1), (1,1,1), (1,0,0)])
        tetrahedrons = [[(0,0,0), (0,1,1), (1,1,0), (0,1,0)],
                [(0,0,1), (1,1,1), (1,0,0), (1,0,1)], *prism_tetra]
    elif triangle_cut["r"]=="01->10" and triangle_cut["tht"]=="00->11":
        prism_tetra = _tri_antiprism_tetrahedrons([
            (1,0,0), (0,0,1), (0,1,0), (1,0,1), (0,1,1), (1,1,0)])
        tetrahedrons = [[(1,0,0), (0,0,1), (0,1,0), (0,0,0)],
                [(1,0,1), (0,1,1), (1,1,0), (1,1,1)], *prism_tetra]
    elif triangle_cut["r"]=="00->11" and triangle_cut["tht"]=="01->10":
        prism_tetra = _tri_antiprism_tetrahedrons([
            (0,0,0), (1,0,1), (0,1,1), (1,0,0), (1,1,1), (0,1,0)])
        tetrahedrons = [[(0,0,0), (1,0,1), (0,1,1), (0,0,1)],
                [(1,0,0), (1,1,1), (0,1,0), (1,1,0)], *prism_tetra]
    else:  # triangle_cut["r"]=="01->10" and triangle_cut["tht"]=="01->10"
        prism_tetra = _tri_antiprism_tetrahedrons([
            (0,1,0), (1,1,1), (0,0,1), (1,1,0), (1,0,1), (0,0,0)])
        tetrahedrons = [[(0,1,0), (1,1,1), (0,0,1), (0,1,1)],
                [(1,1,0), (1,0,1), (0,0,0), (1,0,0)], *prism_tetra]

    for r in range(rs):
        for tht in range(thts):
            for phi in range(phis):
                for i in range(6):
                    subvols[i] = _tetrahedron_volume(wv[r,tht,phi],
                                                     tetrahedrons[i])
                    vols[r, tht, phi] = np.abs(subvols).sum()
    return vols

# https://en.wikipedia.org/wiki/Tetrahedron#Irregular_tetrahedra
def _tetrahedron_volume(cell, indices):
    det_mat = np.empty((3,3))
    det_mat[0] = cell[indices[0]] - cell[indices[3]]
    det_mat[1] = cell[indices[1]] - cell[indices[3]]
    det_mat[2] = cell[indices[2]] - cell[indices[3]]
    return np.linalg.det(det_mat)/6

# converts antiprism to 4 tetrahedron indices
# indices are given as upper1, upper2 upper3, lower1 lower2 lower3 with
# lower1 being the index connecting to upper1 and upper2
# and lower2 to upper2 and upper3
def _tri_antiprism_tetrahedrons(indices):
    u1, u2, u3, l1, l2, l3 = indices
    # cut into two parts along u1, u3, l2, l1 with crease edge as l1, u3
    # and then into two tetrahedrons
    return [[u1, u3, l1, l3], [l3, l1, u3, l2],
            [l1, u1, u3, u2], [l1, l2, u3, u2]]
```

References

[1] L. Boltzmann and B.F. McGuinness. *Theoretical Physics and Philosophical Problems*. D. Reidel Publishing Company, 1974.

[2] Malcolm W Chase and National Information Standards Organization (US). *NIST-JANAF thermochemical tables*, volume 9. American Chemical Society Washington, DC, 1998.

[3] Isabella Milch, Dagmar Aalden, Karin Hirl, Monika Treske. Einführung in die fusionsforschung. `https://www.ipp.mpg.de/46732/3_berichte` or `https://www.ipp.mpg.de/47334/berichte.pdf`, 2003. Accessed: 2022-09-29.

[4] Gerald North. *Stellar Death*, pages 266–277. Macmillan Education UK, London, 1988.

[5] R. et al. Schneider. Plasma edge physics with b2-eirene. *Contributions to Plasma Physics*, 46(1-2):3–191, 2006.

[6] Stroth U. *Plasmaphysik*. Springer Spektrum Berlin, 2018.

[7] Thomas Pütterich. *Control and diagnostic of high-z impurities in fusion plasmas*. habilitation, Ludwig-Maximilians-Universität München, 2015.

[8] Thomas Sunn Pedersen et al. Confirmation of the topology of the wendelstein 7-x magnetic field to better than 1:100,000. *Nature Communications*, 7:13493–13493, 2016.

[9] John Wesson. *Tokamaks*. Oxford University Press, Great Clarendon Street, Oxford ox2 6dp, 2011.

[10] Thilo Romba. Validation of the w7-x cxrs for impurity density profiles. Master's thesis, Eindhoven University of Technology, October 2021.

[11] Allen H. Boozer. Physics of magnetically confined plasmas. *Rev. Mod. Phys.*, 76:1071–1141, Jan 2005.

[12] Samuel A Lazerson, Yu Gao, Kenneth Hammond, Carsten Killer, Georg Schlisio, Matthias Otte, Christoph Biedermann, Monica Spolaore, Sergey Bozhenkov, Joachim Geiger, et al. Tuning of the rotational transform in wendelstein 7-x. *Nuclear Fusion*, 59(12):126004, 2019.

[13] Yuhe Feng, M Jakubowski, R König, M Krychowiak, M Otte, F Reimold, D Reiter, O Schmitz, D Zhang, CD Beidler, et al. Understanding detachment of the w7-x island divertor. *Nuclear Fusion*, 61(8):086012, 2021.

[14] P. C. Stangeby. *The Plasma Boundary of Magnetic Fusion Devices*, volume 2. Taylor & Francis Ltd, 2000.

[15] VP Budaev. Results of high heat flux tests of tungsten divertor targets under plasma heat loads expected in iter and tokamaks. *Physics of Atomic Nuclei*, 79(7):1137–1162, 2016.

[16] Y Feng, M Kobayashi, T Lunt, and D Reiter. Comparison between stellarator and tokamak divertor transport. *Plasma Physics and Controlled Fusion*, 53(2):024009, jan 2011.

[17] S. Chapman, T.G. Cowling, D. Burnett, and C. Cercignani. *The Mathematical Theory of Non-uniform Gases: An Account of the Kinetic Theory of Viscosity, Thermal Conduction and Diffusion in Gases*. Cambridge Mathematical Library. Cambridge University Press, 1990.

[18] S. I. Braginskii. Transport Processes in a Plasma. *Reviews of Plasma Physics*, 1:205, January 1965.

[19] Sydney Chapman and T. G. Cowling. The mathematical theory of non-uniform gases: an account of the kinetic theory of viscosity, thermal conduction, and diffusion in gases. In *The mathematical theory of non-uniform gases*, 1952.

[20] Y Feng, F Sardei, J Kisslinger, P Grigull, K McCormick, and D Reiter. 3d edge modeling and island divertor physics. *Contributions to Plasma Physics*, 44(1-3):57–69, 2004.

[21] Y Feng, F Sardei, and J Kisslinger. 3d fluid modelling of the edge plasma by means of a monte carlo technique. *Journal of Nuclear Materials*, 266-269:812–818, 1999.

[22] Heinke Gerd Frerichs. *3D numerische Parameterstudien zumVerunreinigungstransport in TEXTOR-DED*. PhD thesis, RWTH Aachen, Aachen, Germany, October 2006.

[23] D. Reiter. Randschicht-Konfiguration von Tokamaks: Entwicklung und anwendung stochastischer Modelle zur Beschreibung des Neutralgastransports. Technical Report Juel-1947, Uni. Düsseldorf, Jülich, 1984.

[24] D. Reiter. *The EIRENE Code User Manual*, September 2019.

[25] Jean Zinn-Justin. Stochastic Differential Equations: Langevin, Fokker–Planck Equations. In *Quantum Field Theory and Critical Phenomena*. Oxford University Press, 06 2002.

[26] Alexandros Syrakos, Stylianos Varchanis, Yannis Dimakopoulos, A. Goulas, and John Tsamopoulos. A critical analysis of some popular methods for the discretisation of the gradient operator in finite volume methods. *Physics of Fluids*, 29, 06 2016.

[27] Matthieu Jacobs. Towards the integration of drifts in £d plasma simulation codes with emc3-eirene. Master's thesis, KU Leuven, 2022.

[28] Boris V Chirikov. A universal instability of many-dimensional oscillator systems. *Physics Reports*, 52(5):263–379, 1979.

[29] T. Klinger et al. Overview of first wendelstein 7-x high-performance operation. *Nuclear Fusion*, 59(11):112004, jun 2019.

[30] George Bekefi. *Radiation processes in plasmas*. Wiley, New York, NY, 1966.

[31] Bernd Kurzan. *Untersuchung der Plasmabremsstrahlung im nahen Infrarot zur Bestimmung der effektiven Ionenladungszahl und der Regelung der Elektronendichte in Tokamaks*. PhD thesis, Max Planck Institut für Plasmaphysik, 8046 Garching bei München, Germany, October 1990.

[32] D. Moseev, J.W. Oosterbeek, A. Sirinelli, Y. Corre, M. Houry, S.B. Korsholm, H.P. Laqua, S. Marsen, M. Preynas, J. Rasmussen, M. Salewski, T. Stange, and V. Udintsev. Stray radiation energy fluxes in iter based on a multiresonator model. *Fusion Engineering and Design*, 172:112754, 2021.

[33] Johan W. Oosterbeek, Victor S. Udintsev, Franco Gandini, Matthias Hirsch, Heinrich P. Laqua, Nick Maassen, Yunxing Ma, Alexei Polevoi, Antoine Sirinelli, George Vayakis, and Mike J. Walsh. Loads due to stray microwave radiation in iter. *Fusion Engineering and Design*, 96-97:553–556, 2015. Proceedings of the 28th Symposium On Fusion Technology (SOFT-28).

[34] H Meister, M Willmeroth, D Zhang, A Gottwald, M Krumrey, and F Scholze. Broad-band efficiency calibration of iter bolometer prototypes using pt absorbers on sin membranes. *Review of Scientific Instruments*, 84(12):123501, 2013.

[35] D. Zhang, R. Burhenn, R. Koenig, L. Giannone, P. A. Grodzki, B. Klein, K. Grosser, J. Baldzuhn, K. Ewert, V. Erckmann, M. Hirsch, H. P. Laqua, and J. W. Oosterbeek. Design criteria of the bolometer diagnostic for steady-state operation of the w7-x stellarator. *Review of Scientific Instruments*, 81(10):10E134, 2010.

[36] About adas. `open.adas.ac.uk/about-adas`. Accessed: 2022-06-23.

[37] K. F. Mast, J. C. Vallet, C. Andelfinger, P. Betzler, H. Kraus, and G. Schramm. A low noise highly integrated bolometer array for absolute measurement of vuv and soft x radiation. *Review of Scientific Instruments*, 62(3):744–750, 1991.

[38] Daihong Zhang, Rainer Burhenn, Craig D Beidler, Yuhe Feng, H Thomsen, Christian Brandt, Stefan Buller, Felix Reimold, Philipp Hacker, Ralph Laube, et al. Bolometer tomography on wendelstein 7-x for study of radiation asymmetry. *Nuclear Fusion*, 61(11):116043, 2021.

[39] *Towards integrated data analysis of divertor diagnostics with ray-tracing*, 44th EPS Conference on Plasma Physics, Belfast, Northern Ireland UK, 2017.

[40] David Bold, Felix Reimold, Holger Niemann, Yu Gao, Marcin Jakubowski, Carsten Killer, Victoria R Winters, et al. Parametrisation of target heat flux distribution and study of transport parameters for boundary modelling in w7-x. *Nuclear Fusion*, 62(10):106011, 2022.